

The IAC-Bartol Cosmic Microwave Background Anisotropy

Experiment: Results of the 1994 Campaign

B. Femenía^{1,3}, R. Rebolo^{1,4}, C.M. Gutiérrez^{1,5}, M. Limon^{2,6}, L. Piccirillo^{2,7}

Received _____; accepted _____

¹Instituto de Astrofísica de Canarias, 38200 La Laguna, Spain

²Bartol Research Institute, University of Delaware, Newark, DE 19716

³bfemenia@ll.iac.es

⁴rrl@ll.iac.es

⁵cgc@ll.iac.es

⁶limon@pupgg.princeton.edu

⁷picciril@wisp5.physics.wisc.edu

ABSTRACT

We present the results of a Cosmic Microwave Background (CMB) anisotropy ground-based millimetric experiment sensitive to fluctuations on angular scales of $\sim 2^\circ$. Four independent bands centered at 3.3, 2.1, 1.3 and 1.1 mm collected ~ 550 hours of observation during the Summer of 1994. The instrument was located on the island of Tenerife at an altitude of 2400 m. The low water-vapor content and the atmospheric stability of the site, combined with new techniques to subtract atmospheric noise, result in the reduction of atmospheric contamination in the lowest frequency channel to a level of ~ 1.5 times the instrument noise. Detailed estimations of Galactic foreground contamination show that this contribution is negligible at $|b| \gtrsim 12^\circ$. Two different multipole bands ($\ell = 53_{-13}^{+22}$ and 33_{-13}^{+24}) are analyzed showing that our technique to subtract the atmospheric contribution is more effective in the multipole band at $\ell = 53$. A likelihood analysis of these data reveals the presence of a common signal between the channels at 3.3, 2.1 and 1.3 mm corresponding to a band power estimate of $\sqrt{\bar{\ell}(\bar{\ell} + 1)C_{\bar{\ell}}/(2\pi)} = 2.0_{-0.8}^{+1.0} \cdot 10^{-5}$ and $\sqrt{\bar{\ell}(\bar{\ell} + 1)C_{\bar{\ell}}/(2\pi)} = 4.1_{-2.2}^{+2.4} \cdot 10^{-5}$ for the $\ell = 53$ and 33 multipole bands respectively. Calibration uncertainty has been treated as a systematic effect. The level of fluctuations in the $\ell = 53$ band is in good agreement with our preliminary analysis presented in Piccirillo *et al.* 1997, with measurements by other experiments working at similar angular scales, and with the predictions of standard Cold Dark Matter (CDM) models.

Subject headings: Cosmology: cosmic microwave background - Observations

1. INTRODUCTION

In recent years the COBE DMR (Bennett *et al.* 1996), FIRS (Ganga *et al.* 1993) and Tenerife (Hancock *et al.* 1994) experiments have successfully detected anisotropy at large angular scales yielding precise estimations of the overall normalization of the power spectrum (Hancock *et al.* 1997a) and its shape at low multipole moments $\ell \lesssim 30$. At smaller angular scales ($\ell \gtrsim 70$) a wealth of experiments have reported detections of anisotropy (for an up-to-date list of experimental results see Tegmark’s web site: <http://www.sns.ias.edu/~max/cmb/experiments.html>). These detections clearly suggest a increase in the power spectrum at $\ell \sim 200$ (Netterfield *et al.* 1997, Hancock *et al.* 1997b) and its decline at $\ell \sim 400$ (Scott *et al.* 1996). The main aim of our experiment (for preliminary results see Piccirillo *et al.* 1997) is to fill the gap in ℓ -space remaining between the two ℓ -space regions described above. Thus, with our observing strategy we are probing the multipole bands at $\ell = 33_{-13}^{+24}$ and $\ell = 53_{-13}^{+22}$, in between the Tenerife experiment at $\ell = 20 \pm 8$ (Hancock *et al.* 1997a) and the ACME South Pole at $\ell = 68_{-32}^{+38}$ (Gundersen *et al.* 1995).

The choice of the observing frequencies also distinguishes this experiment from other ground-based experiments. It is known that the combined contributions from Galactic foregrounds and discrete radio sources reaches its minimum at about 55 GHz. However, the presence of a strong O_2 absorption line in the range 50-70 GHz, and the increasing atmospheric emission at millimetric wavelengths hamper observations at these frequencies forces ground-based experiments to observe at cm wavelengths where contamination from synchrotron and free-free emission are of concern. Thus, the millimetric range has been traditionally exploited by satellite and balloon experiments, and only very few ground-based experiments have observed at these frequencies (Python (Platt *et al.* 1997), SuZIE (Church *et al.* 1997) and Andreani *et al.* 1991).

In section 2 we briefly describe the instrument and concentrate on the measurement technique. In section 3 we give the details of the observations. Atmospheric effects in our data are described in section 4. The details of the atmospheric noise reduction technique and the resulting final data sets are presented in section 5. In section 6 we conclude that at high $|b|$ the only expected signal is the CMB. Section 7 describes the statistical data, and conclusions are presented in section 8.

2. INSTRUMENTAL SET-UP AND MEASUREMENT TECHNIQUE

The instrument has been described in detail in previous work (Piccirillo 1991; Piccirillo & Calisse 1993). The optics forms an off-axis Gregorian telescope with a parabolic primary mirror (45 cm diameter) and a hyperbolic secondary mirror (28 cm diameter). The detector is a four-channel photometer equipped with ^3He bolometers working at 0.33K. The bands peak at 3.3, 2.1, 1.3 and 1.1 mm wavelengths (channels 1, 2, 3 and 4 respectively). The beam response for all channels can be well approximated by a Gaussian with $\text{FWHM} = 2.^\circ 03 \pm 0.^\circ 09$ and no significant sidelobes are found.

In addition to the optics, the response of the instrument to a point-like source depends on the observing strategy and demodulation of the data (White & Srednicki 1995). The observing strategy consists in daily drift scans at constant declination achieved by fixing the telescope in azimuth (ϕ) and elevation (θ). Additionally the beam moves on the sky as the primary mirror wobbles sinusoidally while the secondary is fixed. The right ascension (α) and declination (δ) at which the antenna is pointing at time t are given in a good approximation by: $\delta(t) = \delta_0$ and $\alpha(t) = \alpha_0 + \beta_0 / \cos(\delta_0) \times \sin(2\pi f_w t + \epsilon)$, where (α_0, δ_0) is the initial position of the antenna, $\beta_0 = 2.6^\circ$ is the zero-to-peak chopping amplitude at a reference frequency $f_w = 4$ Hz and ϵ is an irrelevant phase constant. Each bolometer's output is sampled at $f_s = 80$ Hz coherently with the mirror movement so to have 20

samples per mirror oscillation. The signal is demodulated in software by evaluating the amplitude of the first (4 Hz) and second (8 Hz) harmonic of the reference frequency f_w . Each demodulation (1F and 2F for the first and second harmonic respectively) can be divided in two components: the in-phase component containing mostly the sky-signal coherent with the reference motion plus the instrument noise and the out-phase containing mostly the instrument noise plus other sources of systematic noise. Such division requires a careful choice of phase which was obtained from observation of the Moon transiting the instrument beam. Then the mapping function at a sky location of coordinates (α, δ) when the antenna is pointing towards (α_0, δ_0) is computed as (White & Srednicki 1995):

$$M_{nF}(\alpha, \delta; \alpha_0, \delta_0) = \frac{N_n}{\sqrt{2\pi}\sigma^2} f_w \int_{-1/(2f_w)}^{1/(2f_w)} dt \cos(n 2\pi f_w t + \zeta) \exp\left[-\frac{\Delta^2(t)}{2\sigma^2}\right] \quad (1)$$

for $n = 1, 2$ indicating respectively the 1F and 2F demodulation, $\sigma = FWHM/\sqrt{8 \ln 2}$, ζ is a phase constant, $\Delta(t)$ is the angular distance between the point of coordinates (α, δ) and the center of the beam at time t and N_n is a normalization constant for the n demodulation obtained by requiring an output of 1 K when the input is an extended source of 1 K filling the positive lobe.

The response of the 1F and 2F demodulations resembles the usual 2-beam and 3-beam responses to the transit of a point-like source through the beam. The 1F demodulated data are well fitted by a 2-beam response with asymmetric Gaussians with $\sigma_\alpha = 1.^{\circ}03$ in the RA direction and $\sigma_\delta = 0.^{\circ}86$ in the declination direction, and with a beam throw of $\beta_0 = 2.^{\circ}38$. The 2F demodulated data are fitted by a 3-beam response with $\sigma_\alpha = 1.^{\circ}56$, $\sigma_\delta = 0.^{\circ}86$ for the positive lobe, and $\sigma_\alpha = 0.^{\circ}89$, $\sigma_\delta = 0.^{\circ}86$ for the negative lobes and a beam throw of $\beta_0 = 2.^{\circ}40$. Additionally, these fits must be multiplied by the factors $\aleph_{1F} = 0.362$ and $\aleph_{2F} = 0.593$ to yield the normalizations to the actual response functions for 1F and 2F respectively. These approximations greatly simplify the statistical analyses

as discussed in section 7.

The response of the instrument to different angular scales (represented in terms of the corresponding multipole moment ℓ) is completely specified by the window function. For a constant declination observation the window function for the product of two temperatures separated by an angle ψ is computed according to White & Srednicki 1995 to give:

$$W_{\ell}(\psi)_{nF} = N_n^2 B_{\ell}^2(\sigma) \sum_{r=0}^{\ell} \frac{(2\ell - 2r)!(2r)!}{[2^{\ell} r!(\ell - r)!]^2} J_n^2[(\ell - 2r)\beta_0] \cos[(\ell - 2r)\psi] j_0^2 \left[\frac{(\ell - 2r)\Delta\Phi}{2} \right] \quad (2)$$

where B_{ℓ} refers to the beam profile: $B_{\ell}(\sigma) = \exp[-\ell(\ell + 1)\sigma/2]$, J_n is the n-th order Bessel function of the first kind, j_0 is the zeroth-order spherical Bessel function and $\Delta\Phi$ is the bin size in radians on the sky. In figure 1 we show the window functions for $\psi = 0$ and $\Delta\Phi = 4$ min in RA, corresponding to the ℓ -ranges $\ell_{1F} = 33_{-13}^{+22}$ and $\ell_{2F} = 53_{-15}^{+22}$. The central value corresponds to the band power average and the upper and lower limits give the ℓ ranges where $W_{\ell}(0)_n$ has amplitudes larger than $e^{-1/2}$ times its peak.

3. CALIBRATION AND OBSERVATIONS

Laboratory calibrations were performed by placing blackbody radiators at different temperatures in front of the optical window. By means of an off-axis mirror the optics within the cryostat is redirected towards a vessel containing eccosorb and divided in four sections. Two sections were filled with liquid Nitrogen alternately placed between the other two sections which were filled with liquid Oxygen. A measurement of the pressure at which these two liquids evaporate gives a precise measurement of the temperature. Then the container is rotated at 2 revolutions per second so the detectors see two black bodies of known temperatures. The calibration factors thus obtained have uncertainties ranging from 1.5% (Channel 1) up to 7.6% (Channel 4). Since we are concerned with the possibility of

systematic effects in the calibration process we quote a laboratory calibration uncertainty based on our observations of the Moon (see below).

Our observations were conducted during June and July 1994, collecting about 550 hours of data, at Observatorio del Teide at Tenerife (Spain). The site, at an altitude of 2400 m and latitude N 28°29', is well known among the solar community for its good seeing and the large percentage of clear days, the latter due to the fact that the inversion layer lies below the observatory for about 75 % of the time. This is also the location of the Tenerife experiment (Hancock *et al.* 1994) which has already demonstrated the potential of the site for hosting observations in the cm range due to the stability of the atmosphere and its excellent transparency (Davies *et al.* 1996). These features makes of this site a promising place for mm observations.

The observations concentrated at declination $\delta = 40^\circ$ by pointing the antenna towards the North meridian and at an elevation angle of $h = 78^\circ.7$. This declination has been extensively measured from this site at larger angular scales ($\sim 5^\circ$) and lower frequencies (10, 15 and 33 GHz) with reported detections of structures in the CMB by the Jodrell Bank-IAC experiments (Hancock *et al.* 1994; Gutiérrez *et al.* 1997).

The measurements started after the Sun was well below the horizon in order to avoid solar contamination. The angular distance between Moon and beam was always greater than $23^\circ.5$ for the $\delta = 40^\circ$ observations. In addition the Moon was observed for astronomical calibration. The values obtained from the analysis of the Moon transits in the 1F demodulation agree within $\sim 20\%$ of the laboratory calibrations for all channels (see figure 2). The bulk of the calibration uncertainty (6 %, 26 %, 22 % and 10 % for channels 1, 2, 3 and 4 respectively) we believe is due to the lunar models used (Bennett *et al.* 1992a, Hagfors 1970). By fitting the observed Moon transit to the expected transits at both demodulations, and modeling the Moon as an extended uniform disk and the beam

as Gaussian shaped, we obtain estimates for the beam width, σ , and chopping amplitude, β_0 , given in table 1. Since the Moon transit is better defined in the 1F data we adopt the estimates for σ and β_0 from the 1F demodulation. The values for β_0 from the fits to each channel are consistent with each other, yielding an average value of $\beta_0 = 2^\circ.90 \pm 0^\circ.03$. As expected, the beam widths seen by each channel show a monotonic decrease with frequency so that channel 1 has the widest beam and channel 4 the narrowest beam. Even so, given the sizes of the error bars assigned to each width, all of them are consistent with a unique beam width given by the weighted average: $\bar{\sigma} = 0^\circ.86 \pm 0^\circ.04$. In any case, for calibration purposes we adopted for each channel the best fit value obtained for that channel. It is worth mentioning the agreement between the FWHM estimated for channel 1 in the lab ($FWHM = 2^\circ.40 \pm 0^\circ.10$) with that from the fit to the Moon transit ($FWHM = 2^\circ.21 \pm 0^\circ.24$ from the 1F Moon transit and $FWHM = 2^\circ.4 \pm 0^\circ.6$ from the 2F Moon transit). The discrepancy between the values of β_0 measured in the lab and from the Moon transit can only be attributed to the antenna assembling, and throughout this work we have assumed the value of β_0 as obtained from the Moon transit analysis.

4. ATMOSPHERIC EFFECTS ON THE DATA

The biggest source of noise for CMB ground observations at millimetric wavelengths comes from atmospheric emissions dominated by fluctuations of O_2 and water vapor contents. Given the stability of the pressure during the campaign, the most important parameter turned out to be the precipitable water vapor. The meteorological conditions during the campaign are summarized in figure 3. The pressure and temperature are measured at the observatory four times a day. The relative humidity is also measured at the observatory every few minutes. The precipitable water vapor is obtained from the measurements of the balloons launched twice a day by the Spanish Meteorological Institute

from sea level. In our case, the precipitable water vapor is obtained by integrating the balloon measurements from the Observatory level up to 12 – 15 Km.

4.1. ATMOSPHERIC NOISE LEVELS VS INSTRUMENT NOISE LEVELS

Atmospheric effects in our data become evident as a big increase with respect to the expected instrument noise levels. In the ideal case (i.e. the instrument noise is white) we should observe flat power spectra if our data were entirely due to instrumental noise. However our data are a combination of instrument noise, atmospheric noise and astronomical signal, the latter to be ignored given its weakness in each night of observation. At low frequencies neither the instrument noise nor the atmospheric noise exhibit flat spectra. Bolometers show a characteristic $1/f$ spectrum while atmospheric fluctuations have a more complicated spectrum and in general follow a $1/f^k$ spectrum with k variable. On the other hand, both spectra flatten at high frequencies, becoming indistinguishable from each other. At high frequencies the power spectra are flat, and assigning to the instrument noise the value corresponding to such noise floor is a huge overestimation.

In theory, this problem could be solved by using the out-phase component produced during the demodulation because it is expected to contain only instrumental noise. In practice, even in the out-phase component there are still residual amounts of atmospheric noise because it is impossible to find a constant demodulation phase which completely sets to zero the sky-signal in the out-phase component. In figure 4 we show the noise spectra in thermodynamic temperature for all channels and both demodulations of the in- and out-phase components for a typical night of observation. Channel 1 exhibits power spectra almost flat in the out-phase spectra for 1F and 2F demodulations, indicating that most of the noise in channel 1 at high frequencies is due to instrument noise. The out-phase components for the rest of the channels still contains considerable amounts of

atmospheric noise as indicated by the similar shapes of the spectra in the in- and out-phase components. This interpretation is strongly supported by the fact that the spectral shape at low frequencies, and the noise floor at high frequencies, change from day to day. The higher values for the instrumental noise as obtained from the analysis of the out-phase components of the the 1F data indicate the greater ability of the 2F demodulation in removing linear gradients caused by atmospheric emission . The final upper limits in thermodynamic units assigned to the instrument noise are 2.8, 0.8, 1.5 and 1.0 mK s^{1/2} for channels 1 to 4 as obtained from the analysis of the out-phase components of the 2F demodulation. In figure 5 we show the distribution of the *rms* values, calculated over 30 minute intervals, with 10 second bins for all channels and both demodulations. At 10 seconds the contribution from instrument noise to the *rms* would be less than 1mK for all channels, so most of the noise must be atmospheric. The noise level and the width of its distribution are larger in the 1F demodulation. Additionally, the minimum values obtained in the 2F data are smaller; another indication of the enhanced ability of the 2F demodulation to reduce atmospheric noise.

4.2. ATMOSPHERIC CORRELATIONS IN THE DATA

The second relevant effect due to atmospheric contamination concerns correlation between different channels. This is evident from the highly correlated time-variable signals seen by all channels for the same night of observation. This point will be used subsequently on as the cornerstone for our analysis to reduce atmospheric noise in the data. In table 2 we present the mean correlation between channel i ($i = 1, 2, 3$) and channel 4 for the whole campaign and for the data selected to build the final data sets. As expected this correlation increases when increasing the frequency of channel i and it is higher in the 1F data than in the 2F data.

Another effect is the auto-correlation introduced by atmospheric noise. Primary evidence of this effect is that the *rms* of the data do not follow the $1/\sqrt{N}$ law when the data are binned. We have computed the auto-correlation function for the data within the same night of observation as seen by each channel at both demodulations. This was done by using the power spectra of the in-phase components and the Wiener-Khinchin relations (see e.g. Barkat 1991). As noticed when computing the instrument noise limits, the in-phase component power spectra show a large departure from white noise, implying non-zero auto-correlations at lags different from zero. The average auto-correlation function for the whole campaign and for all channels and both demodulations is shown in figure 6. For a given lag we observe that the auto-correlation function is always larger in the high frequency channels. The coherence time is always larger for the 1F data than for the 2F data. This reflects the higher efficiency with which a double-switching technique is able to discard the effects of linear temporal drifts due to atmospheric emission. From figure 6 we conclude that it is necessary to use bins large enough such that correlation between adjacent bins is reduced (see section 5). This will ensure that the standard deviations are properly computed and assigned as error bars when moving to larger bin sizes.

5. DATA PROCESSING

The demodulation process produces a data point every 0.25 s per each 1F and 2F demodulation and per channel. During the demodulation 3.3% of the data was rejected due to problems of synchronism between the mirror movement and the data acquisition system. The bulk of the data rejection was performed during the subsequent phases of binning and editing comprising the data processing. After demodulation a binning is performed to bring the data from 0.25 s to 10 s. This is a trade-off between the need to reduce correlation between adjacent bins (auto-correlation $< 65\%$ for all channels at 1F demodulation and

< 35% for all channels at 2F demodulation) and to have a large enough number of points for the linear fits and further binning processes involved in the cleaning technique. During the 0.25 s to 10 s binning an iterative 3σ filter is applied three times to discard glitches due to malfunctions of the data acquisition system. Bins of 10 s built with 15 or less points at 0.25 s are also discarded. In total, the amount of data rejected in this binning is about 8% for all channels and both demodulations.

As explained in the section 4, the extremely large temporal correlation between all channels and the amplitudes and behavior of the noise levels with the bin size strongly support the atmospheric origin of the bulk of the noise in our data. Hence, the primary goal of any data reduction concerns the assessment and subtraction/reduction of this unwanted source of noise.

5.1. DESCRIPTION OF THE CLEANING TECHNIQUE

The approach adopted in this work consists in exploiting the high correlation between channels as an indicator of the atmospheric emission, so that by using a channel as a monitor we can clean the rest of the channels. Since channel 4 (1.1 mm band) is the most sensitive to atmospheric emission, we adopt it as the monitor. The method assumes that at each channel i we have a superposition of astronomical signal attenuated by f_i due to the atmospheric transparency, plus the contribution from the atmospheric emission. When expressing all quantities in antenna temperature we have at channel i : $\Delta T_{ANT,i} = f_i \Delta T_{ANT,i}^{astro} + \Delta T_{ANT,i}^{atm}$. We assume that the atmospheric contributions are perfectly correlated between different channels so: $\Delta T_{ANT,i}^{atm} = \alpha_i \Delta T_{ANT,4}^{atm}$. This assumption is strongly justified given the high correlation between data at different channels taken during the same night of observation (see table 2). The amplitude of the signals are too high to be attributed to CMB signal or other astronomical signal (see section 6) giving additional support to the above assumption.

To recover the astronomical signal at channel i in thermodynamic temperature (ΔT_i^{astro}) and referred to the top of the atmosphere we solve the linear equation:

$$\Delta T_{ANT,i} = \frac{f_i}{c_i} \Delta T_i^{astro} + \left(\Delta T_{ANT,4} - \frac{f_4}{c_4} \frac{1}{\rho_{i4}} \Delta T_i^{astro} \right) \times \alpha_i \quad (3)$$

where $\Delta T_{ANT,i}$ and $\Delta T_{ANT,4}$ are the recorded antenna temperatures at channels i and 4 respectively; f_i and f_4 the atmospheric attenuation factors; c_i and c_4 are the Rayleigh-Jeans to thermodynamic conversion factors: $\Delta T_{ANT,i} = \frac{1}{c_i} \Delta T_i$ ($c_i = 1.29, 1.66, 3.66, 4.82$ for channels 1 to 4 respectively) and ρ_{i4} is the fraction of the astronomical signals seen at channels i and 4. The second term within the parenthesis accounts for common structure in channels i and 4, though with different amplitudes. Based on our estimations of non-CMB contaminants, at high Galactic latitude (high $|b|$) we expect no astronomical signal other than the CMB itself (see section 6) so $\rho_{i4} = 1$. At low $|b|$ and in the Galactic plane we expect different signals in shape and in amplitude as seen by different channels. This motivates the introduction of $\rho_{i4} \neq 1$, whose value is obtained from our estimations of the Galactic diffuse emission.

The atmospheric cleaning technique is applied to the 10s-binned data after subtraction of a constant offset from each channel. The rejected data typically correspond to sections taken during bad weather and/or warming of the cryostat. The data are divided into segments of 5 minutes. For each of these segments we compute the values of α_i from a linear fit of channel i versus channel 4. Likewise, all points within the same 5 minute segment share the same f_i and f_4 as computed from the splined values of water vapor w , pressure P and temperature T from figure 3 used as input to the code by Cernicharo 1985, which computes the atmospheric opacities due to water vapor and oxygen using the US standard atmosphere model.

5.2. PRODUCING THE FINAL DATA SETS

After cleaning, a new binning is performed to bring each processed night of observation from a 10 second to a 4 minute bin size so the beam is sampled with at least 3 points. Once again a 3σ filter is applied to discard possible glitches occurred during the cleaning process. To each point at 4 minutes we assign an error bar given by the standard deviation of the mean of all points at 10s within the bin at 4 minutes. A similar analysis to that performed in section 4.2 allows us to obtain the mean auto-correlation function for the processed data in each channel and both demodulations. This analysis shows that for points separated by 4 minutes the auto-correlation functions for all channels 1 to 3 and both demodulations range between 9% (Ch 2 1F) and 1% (Ch 1 2F). Therefore, our 4 minute bins can be considered uncorrelated as well as their error bars. In both demodulations and in all channels we observe residual baselines of very long periods. We proceed to remove these remnants by fitting linear combinations of sinusoidal functions after a re-edit of the data. The re-edit discards noisy sections which may affect the fitting process. The minimum period of the sinusoidal functions is chosen to be large enough so to remove signals corresponding to angular scales bigger than the ones to which the instrument is sensitive. Thus, for the 1F data the minimum period is 90° in RA and a minimum period of 72° in RA for the 2F data. In figure 7 we display these various stages of the cleaning technique for a typical night as seen in all channels and both demodulations. In the last column of table 3 we give the mean amplitude of the baseline fits. Columns 1 and 2 show the percentage of total data used with respect to the original data at 0.25 s and the number of nights used to generate the final data sets. The percentage of data used is bigger in the 2F data as well as the number of used nights, with the exception of channel 3. The final data sets were obtained by stacking all individual baseline-cleaned nights where the *rms* did not exceed 0.65, 1.3 and 2.5 mK for channels 1, 2 and 3 respectively in the 1F demodulation and 0.4, 0.4 and 2.0 mK for channels 1, 2 and 3 respectively in the 2F demodulation. Column 3 in table 3

gives the mean *rms* for the surviving nights once residual baselines have been removed. The stacking process consists of computing weighted averages, where to the *i*th bin in the final data set we assign a value and error bar given by:

$$\overline{\Delta T}_i = \frac{\sum_{j=1}^{n_i} \Delta T_{ij} / \sigma_{ij}^2}{\sum_{j=1}^{n_i} 1 / \sigma_{ij}^2} \quad (4)$$

$$\sigma_i^2 = \frac{\sum_{j=1}^{n_i} (\Delta T_{ij} - \overline{\Delta T}_i)^2 / \sigma_{ij}^2}{\sum_{j=1}^{n_i} (n_i - 1) / \sigma_{ij}^2} \quad (5)$$

where the indices *ij* refer to bin *i* in night *j*, ΔT_{ij} and σ_{ij} are the data point and standard deviation at bin *i* in night *j*, and n_i is the number of nights used for this *i*th bin in the final data set. The final data sets in the regions before and after the Galactic Plane crossing are shown in figure 8.

5.3. PERFORMANCE OF THE TECHNIQUE

The efficiency of the atmospheric reduction process is best demonstrated by looking at the power spectra of the data before and after its application. In figure 9 we show the power spectra of both demodulations and for channels 1, 2 and 3 for a typical night before and after cleaning. This figure corresponds to the same data as in figure 4. The reduction in the noise level is evident from these plots, so that the corrected Ch 1 and Ch 2 in both demodulations approach the levels expected from instrument noise. We also notice the flattening, approaching the ideal behavior of white noise. For channel 3 there is also an overall decrement in the power spectra of both demodulations indicating that a substantial fraction of the atmospheric noise has been subtracted. However, the levels of the cleaned data for channel 3 still show residual atmospheric contamination. In table 4 we give the values attained by the noise spectrum in the in-phase components at different frequencies

and for both demodulations before and after cleaning for the same observing night as in figure 9. The corresponding values are also given for the out-phase component spectra. At low frequencies (i.e 0.001 Hz) where atmospheric effects are more evident the cleaned file exhibits lower values of the noise spectra than before cleaning; a good indication that most of the atmospheric noise has been removed. Further, this value approaches the values attained in the out-phase components containing small amounts of atmospheric noise due to the leakage during the demodulation.

Another indication of the performance of the technique is given in figure 10 where we show the distribution of the *rms* values measured in the 10 second binned data after applying our cleaning method. Once again the last bin exhibits a high value since it also contains the contributions from all following bins to avoid a huge spread in the plots. When we compare this figure with figure 5 we notice a huge decrement of the *rms* for all channels and both demodulations.

Another check of the performance is the recovery of the Galactic Plane (GP) crossing. The introduction of a factor $\rho_{i4} \neq 1$ to recover the GP explicitly assumes perfect correlation of this signal as seen by channel i and channel 4. This is a very good approximation for channels 2, 3 and 4 where the bulk of the Galactic emission is due to dust emission. The estimated GP crossings in channel 2 1F demodulation (2F demodulation) is 99% (96%) correlated with channel 4, while the estimation of the GP in channel 3 1F demodulation (2F demodulation) attains a 100% (100%) correlation with respect to the GP seen by channel 4. For channel 1 the contributions from dust and free-free emission are comparable, the latter slightly more important. Furthermore, the free-free template (1420 MHz map) and the dust template (240 μm DIRBE map) show a relative slight displacement in the position of the GP at $\delta = 40^\circ$, thus lowering the correlation between channel 1 and channel 4 down to 93% and 72% for the 1F and 2F data respectively. In figure 11 we show the

predicted Galactic Plane crossings superimposed on our measurements for channels 1, 2 and 3 and both 1F and 2F demodulations. As discussed in section 6, we have considered the dust model in Boulanger *et al.* 1996, with the ρ_{i4} factors listed in table 5. We have also tried several different Galactic emission models in the literature and have checked that, while the absolute amplitudes in each channel depend strongly on the model used, their ratios are quite stable and so is the parameter ρ_{i4} as can be seen in table 5. The slight differences between the ρ_{i4} factors for the 1F and 2F demodulations are not relevant, except for channel 1. This is a direct consequence of the above mentioned displacements between the contributions generating the GP in channel 1. Using ρ'_{i4} in equation (3) instead of ρ_{i4} results in an amplification/attenuation of the restored GP given by:

$$\Gamma_i = \frac{f_i/c_i - \alpha_i \cdot f_4/(c_4 \cdot \rho_{i4})}{f_i/c_i - \alpha_i \cdot f_4/(c_4 \cdot \rho'_{i4})} \quad (6)$$

The extreme values of Γ_i obtained when using the ρ_{i4} values obtained from the models described in table 6 are 0.6 and 1.2. Therefore we do not expect big changes in the amplitude of the restored GP due to the change of dust model used to estimate the values of the ρ_{i4} factors. The general agreement between the predictions and our measurements constitutes an important check on the performance of our system and method.

6. GALACTIC FOREGROUNDS

The Galactic contribution has been analyzed considering the synchrotron, free-free and dust emission. When studying the synchrotron emission it is convenient to distinguish between the expected levels of signal at low galactic latitudes (i.e at $|b| \lesssim 12^\circ$ or GP crossings) and at high galactic latitudes (i.e at $|b| \gtrsim 12^\circ$ or outside the GP).

As studied by Tegmark & Efstathiou 1996, outside the GP and at our angular scales

and frequencies, the contributions from the Galactic synchrotron and free-free emission are expected not to be a source of confusion with CMB anisotropy. We have also conducted a study of the expected levels of contamination by synchrotron and free-free emission in our data by convolving our instrumental response with a template of synchrotron and free-free processes. This template was obtained by extrapolating in frequency from the low frequency map at 1420 MHz (Reich & Reich 1986), and modeling both processes with a single power-law: $T_{ff-sync} \propto \nu^{-\beta}$. The spectral index β is obtained by fitting this law to the low frequency maps at 408 MHz (Haslam *et al.* 1982) and at 1420 MHz. The results of such an analysis predict that free-free plus synchrotron would contribute to the observed *rms* with values smaller than $1 \mu\text{K}$ for both demodulations and in all channels. Additionally, assuming the extremely conservative approach that the signal seen at 33 GHz by the Tenerife experiment is entirely synchrotron emission, and extrapolating with $\beta = 2.7$, we obtain that for all channels the synchrotron emission at high $|b|$ amounts for less than $1\mu\text{K}$ in both 1F and 2F data. These two independent approaches clearly indicate the negligible effect of synchrotron and free-free emission on our data at high $|b|$.

In the GP region the map at 1420 MHz is dominated by free-free emission due to the presence of the Cygnus X HII region and many other unresolved HII regions (Davies *et al.* 1996). Accordingly, when generating the template for this region we assumed a spectral index of $\beta \simeq 2.16$ as obtained from equation (3) of Bennett *et al.* 1992b. To generate the template in this region we also considered the possibility of still having non-negligible contributions of synchrotron emission in the 1420 MHz map as indicated by the spectral indexes required to reproduce the GP's seen by DMR at 31.5, 53 and 90 GHz.

We have used the DIRBE map at $240 \mu\text{m}$ as template for the dust emission and extrapolated to our frequencies by using the fit to the FIRAS data obtained by Boulanger *et al.* 1996 resulting in a model with $n = 2$ and $T_d = 17.5\text{K}$. We have checked the validity

of this model at low $|b|$ by reproducing the expected dust contribution to the GP seen by COBE DMR at 90 GHz where the relevant section has been smoothed to 10° FWHM. Together with a brief description and reference to the dust model used, in table 6 we give the *rms* values expected from synchrotron plus free-free and dust emission for different dust models outside the GP ($|b| \gtrsim 12^\circ$). These *rms* values are completely negligible as compared to the observed *rms* values in our final data sets (see section 7). This can also be seen by using the figure of $\Delta T_{dust} = 2.7 \pm 1.3 \mu K$ at 53 GHz and 10° angular resolution by Kogut *et al.* 1996b.

Of much less concern is the contamination due to unresolved sources and from known point-like sources. The latter contribution was computed by convolving our instrument beam with a grid where we placed sources extracted from the Kühr *et al.* (1981) and the Green Bank sky survey (Condon, Broderick & Seielstad 1989) complemented by the Michigan and Metsahovi monitoring programme. The weakest considered source presents a flux density at 5 GHz of 0.18 Jy. We extrapolate the flux density to our frequencies using the fit obtained by Kühr *et al.* 1981 where available. Fluxes of sources not present in Kühr *et al.* 1981, but for which we have measurements at three different frequencies, were fitted to a power law and extrapolated to our frequencies, while flat spectra were assumed for those sources for which flux densities were available only at a single frequency. For all channels and both demodulations the expected *rms* in the section of our data $|b| > 12^\circ$ is much smaller than $1 \mu K$. Finally we refer to Franceschini *et al.* 1989 to also exclude the contribution from randomly distributed sources given our observing frequencies and beam width. In view of all these figures we conclude that outside the GP the only expected astronomical signal should be CMB.

7. STATISTICAL ANALYSIS

7.1. THE LIKELIHOOD FUNCTION

The data selected for the statistical analysis have been chosen under two requirements. First the selected bins must correspond to regions of high $|b|$ where we are confident that Galactic emission is negligible. Thus we have identified two sections in our data: RA_1 for which $b > +12^\circ$ and RA_2 for which $b < -12^\circ$. The second requirement concerns the number of independent nights (n_i in equations (4) and (5)) used to generate the final data sets. This causes the different RA ranges (columns 1 and 5 in table 7) over which the selected data for each channel and demodulation span. This happens because the different editions and cleaning technique are performed independently for each channel and demodulation. The minimum number of independent nights required is $n_i = 6$, except for channels 1 and 2 in the 2F demodulation where the higher number of used nights allows to increase this threshold up to 9 and 8 points respectively. In all cases the number of points used for generating the final data bins is large enough to allow to use the Kolmogorov-Smirnov test to check that our bins in the final data sets are consistent with being drawn from Gaussian distributions. Then, the likelihood function for a set of data \vec{x} is completely specified by giving the covariance matrix \mathbf{V} and the vector of means \vec{x} , which in our case is identically zero. Then:

$$\mathcal{L} \propto \frac{1}{|\mathbf{V}|^{1/2}} \exp\left(-\frac{1}{2} \vec{x}^T \mathbf{V}^{-1} \vec{x}\right) \quad (7)$$

where $|\mathbf{V}|$ denotes the determinant of \mathbf{V} . There are two independent contributions to the covariance matrix so that $\mathbf{V} = \mathbf{V}_T + \mathbf{V}_D$, where \mathbf{V}_T corresponds to the correlations between bins according to the model we are testing and shows dependence on the parameters to be estimated, and \mathbf{V}_D is the data covariance matrix computed directly from the data. We compute the elements ij of \mathbf{V}_T by assuming an intrinsic Gaussian auto-correlation function (GACF): $\mathbf{V}_{intr}(\theta_{ij}) = C_0 \exp(-\theta_{ij}^2/(2\theta_c^2))$ where θ_{ij} is the angular separation between bins

i and j , θ_c is the coherence angle, the angle of maximum sensitivity for each experimental configuration: $\theta_c = 2.17^\circ$ and $\theta_c = 1.42^\circ$ for the 1F and 2F data respectively and $C_0^{1/2}$ is the parameter to be estimated. We also have to consider the effects introduced by the finite width of the beam and the observing strategy. After convolving with the combination of Gaussian beams reproducing our instrument responses (see section 2), we obtain that the elements (i, j) of the matrices $\mathbf{V}_{T,1F}$ and $\mathbf{V}_{T,2F}$, for the 1F and 2F demodulation respectively, are given by:

$$\begin{aligned} \mathbf{V}_{T,1F}(i, j) &= \aleph_{1F}^2 \times [2 \cdot C_M(\theta_{ij}; \sigma_\alpha, \sigma_\alpha, \sigma_\delta) - C_M(\theta_{ij} + \beta; \sigma_\alpha, \sigma_\alpha, \sigma_\delta) - \\ &C_M(\theta_{ij} - \beta; \sigma_\alpha, \sigma_\alpha, \sigma_\delta)] \end{aligned} \quad (8)$$

$$\begin{aligned} \mathbf{V}_{T,2F}(i, j) &= \aleph_{2F}^2 \times [C_M(\theta_{ij}; \sigma_c, \sigma_c, \sigma_\delta) - C_M(\theta_{ij} + \beta; \sigma_c, \sigma_l, \sigma_\delta) + \\ &\frac{1}{2}C_M(\theta_{ij}; \sigma_l, \sigma_l, \sigma_\delta) - C_M(\theta_{ij} - \beta; \sigma_c, \sigma_l, \sigma_\delta) + \\ &\frac{1}{4}(C_M(\theta_{ij} + 2\beta; \sigma_c, \sigma_l, \sigma_\delta) + C_M(\theta_{ij} - 2\beta; \sigma_c, \sigma_l, \sigma_\delta))] \end{aligned} \quad (9)$$

where $C_M(\theta; \sigma_c, \sigma_l, \sigma_\delta) = C_0 \theta_c^2 / \sqrt{(\theta_c^2 + \sigma_c^2 + \sigma_l^2)(\theta_c^2 + 2\sigma_\delta^2)} \exp[-\theta^2 / (2(\theta_c^2 + \sigma_c^2 + \sigma_l^2))]$ and, as obtained in section 2, $(\sigma_\alpha, \sigma_\delta, \beta, \aleph_{1F}) = (1.^\circ 03, 0.^\circ 86, 2.^\circ 38, 0.362)$ and $(\sigma_c, \sigma_l, \sigma_\delta, \beta, \aleph_{2F}) = (1.^\circ 56, 0.^\circ 89, 0.^\circ 86, 2.^\circ 40, 0.593)$ for the 1F and 2F demodulation respectively.

In a Bayesian interpretation with uniform prior, the likelihood (\mathcal{L}) as a function of the positive definite parameter $C_0^{1/2}$ is directly proportional to the probability density function of $C_0^{1/2}$. Then the best estimation of $C_0^{1/2}$ is that value for which \mathcal{L} is maximum while confidence levels $[(C_0^{1/2})_1, (C_0^{1/2})_2]$ to a C% level have been computed by requiring $\mathcal{L}((C_0^{1/2})_1) = \mathcal{L}((C_0^{1/2})_2)$ and $\int_{(C_0^{1/2})_1}^{(C_0^{1/2})_2} \mathcal{L}(C_0^{1/2}) d(C_0^{1/2}) / \int_0^\infty \mathcal{L}(C_0^{1/2}) d(C_0^{1/2}) = C/100$. In what follows detections are given to a 68% CL, and upper limits to a 95% CL . A claim of

detection is made whenever the lower limit of the confidence interval at 68% CL is not zero, otherwise we quote the upper limit at 95% CL.

7.2. LIKELIHOOD ANALYSIS ON SINGLE CHANNELS

We have applied the likelihood analysis to each channel and demodulation in the ranges: RA_1 , RA_2 and $RA_1 + RA_2$. The results of these analysis are given in table 8. In all cases the values obtained in all these RA ranges are consistent with the presence of a common signal. For channel 2 at 1F demodulation the results between RA_1 and RA_2 are still marginally consistent, but the result in the RA_1 section shows a strong dependence on the choice of individual nights to generate the final data set. Accordingly in what follows we will only consider the RA_2 section for channel 2 at 1F.

For channels 1 and 2, in all valid ranges and in both demodulations, the signals detected are consistent between them and with values of $\sim 100\mu\text{K}$. These values are consistent with our previous results reported in Piccirillo *et al.* 1997, where we concluded that the slight excess of signal seen in channel 2 with respect to that obtained in channel 1 may indicate the presence of some residual levels of atmospheric noise at the same level as the expected CMB signal.

The results obtained for channel 3 at both demodulations clearly indicate that it is still affected by important atmospheric residuals: CMB signal does not scale with frequency and our estimated signals due to diffuse Galactic contamination at channel 3 amount to $C_{0,Gal}^{1/2} < 35\mu\text{K}$, too large a difference to be caused by the uncertainties in the Galactic estimation procedure.

7.3. JOINT LIKELIHOOD ANALYSIS

The joint analysis of all three channels allows us to estimate the most likely signal which is common to all of our frequencies, such as CMB anisotropy. To estimate the correlation between channels we have computed the cross-correlation function between sections of data at 10 s which overlap in the same nights in channels i and j . We make use of the generalized Wiener-Khinchin relations for stationary processes to obtain one cross-correlation curve per night. The average of these curves are plotted in figure 12. We observe that the cross-correlation becomes negligible at scales smaller than our binning in the final data sets, being only significantly different from zero at zero-lags as indicated in columns 2 and 4 in table 9. This cross-correlation at zero-lag enhances the diagonal terms in the sub-matrices which take into account the correlation between different channels in the covariance matrix \mathbf{V}_D . This effect has been analyzed and discussed in detail by Gutiérrez 1997, concluding that the net effect is an increase of the error bars as compared with the case where not such correlations are present. In table 9 we present the results from the joint analysis of any two channels and all three channels for each demodulation. These results have been obtained by using the whole data set except for those involving channel 2 at 1F for which only the RA_2 section of the data set was used.

The analysis on any combination of 2 channels indicates the presence of common signal, which for the 1F demodulation is $C_0^{1/2} \sim 150\mu\text{K}$ and $\sim 75\mu\text{K}$ for the 2F demodulation. Although being completely consistent, these figures must be viewed with caution: the signal monotonically increases as we increase the frequencies of the channels being combined. This behavior again indicates the higher level of contamination in channel 3 for both demodulations.

Finally, we have also considered the case of having a superposition of CMB signal plus a signal with a spectral behavior different from a black-body. In this way we obtain the

contamination due to a foreground component which is consistent with the data. We also assume a GACF with the same coherence angle as the CMB signal for the foreground signal in addition to a scaling of the signal with frequency. Thus the foreground signal in channel 1 exhibits an intrinsic ACF $C_{Ch\ 1}^{Fgd}(\theta) = C_{0,Fgd} \exp[-\theta^2/(2\theta_c^2)]$ while channel j ($j = 2, 3$) shows $C_{Ch\ j}^{Fgd}(\theta) = C_{Ch\ 1}^{Fgd}(\theta) \times (\nu_j/\nu_1)^{2n} \times (c_j/c_1)^2$. As in equation (3) c_i ($i = 1, 2, 3$) is the Rayleigh-Jeans to thermodynamic conversion factor; $\nu_1 = 95.1$ GHz, $\nu_2 = 169.0$ GHz and $\nu_3 = 243.5$ GHz the frequencies for channels 1, 2 and 3 respectively. By setting the value of n to the appropriate values we obtain the signal due to any of the foreground contaminants. The likelihood function now becomes a function of two parameters to be estimated: $\mathcal{L} = \mathcal{L}(C_{0,cmb}^{1/2}, C_{0,Fgd}^{1/2})$. Since, *a priori*, we do not have any information about either of them we obtain the probability distribution function of $C_{0,cmb}^{1/2}$ by marginalizing with respect to $C_{0,Fgd}^{1/2}$ and vice-versa. In table 10 we present the results of this analysis for different values of the spectral index n covering the ranges expected for dust, atmospheric, synchrotron and free-free emission. In figures 13 and 14 we show the contour plots for the spectral indexes $n = 2.0, 0.0, -2.1$ and -3.0 , corresponding to dust, a simple atmospheric model, free-free and synchrotron emission in Rayleigh-Jeans approximation. The data are then converted into thermodynamic units in the plots. Small departures from these nominal values yield essentially the same results as seen in table 10.

7.4. DISCUSSION OF THE RESULTS

The joint analysis of channels 1, 2 and 3 at the 2F demodulation reveals the presence of a common signal with $C_0^{1/2} = 72_{-24}^{+26} \mu\text{K}$. The conversion to band power estimates (e.g. Steinhardt 1994) yields $\sqrt{\bar{\ell}(\bar{\ell} + 1)C_{\bar{\ell}}/(2\pi)} = (2.0 \pm 0.7) \cdot 10^{-5}$ at $\bar{\ell} = 53_{-15}^{+22}$ in good agreement with our previous results in Piccirillo *et al.* 1997 ($C_0^{1/2} = 76_{-21}^{+23} \mu\text{K}$ for a GACF or $\sqrt{\bar{\ell}(\bar{\ell} + 1)C_{\bar{\ell}}/(2\pi)} = (2.1 \pm 0.6) \cdot 10^{-5}$ in the band power estimate

notation). At similar angular scales, $\bar{\ell} = 56_{-18}^{+21}$, Netterfield *et al.* 1997 quote a value of $\sqrt{\bar{\ell}(\bar{\ell} + 1)C_{\bar{\ell}}/(2\pi)} = 1.8_{-0.3}^{+0.7} \cdot 10^{-5}$.

We have also tested the possibility that part of the detected common signal is due to contamination by Galactic foregrounds or residual atmospheric contamination. The analysis confirms that dust can not be responsible of the detected signal ($C_{0,Dust}^{1/2} < 25 \mu\text{K}$), leaving a CMB signal of $C_0^{1/2} = 72_{-22}^{+26} \mu\text{K}$ which corresponds to $\sqrt{\bar{\ell}(\bar{\ell} + 1)C_{\bar{\ell}}/(2\pi)} = 2.0_{-0.6}^{+0.7} \cdot 10^{-5}$. After considering calibration uncertainty as a systematic effect the figures above become $C_0^{1/2} = 72_{-28}^{+34} \mu\text{K}$ and $\sqrt{\bar{\ell}(\bar{\ell} + 1)C_{\bar{\ell}}/(2\pi)} = 2.0_{-0.8}^{+1.0} \cdot 10^{-5}$. Less conclusive is our analysis when a free-free or synchrotron spectrum is assumed for the contaminant signal. Then we only have vague upper limits for the contaminants which were known in advance from both our estimations and results from the Tenerife experiment when observing at $\delta = 40^\circ$. As indicated in section 6, the free-free contamination seen by the Tenerife experiment at 33 GHz is about $4 \mu\text{K}$. The extrapolation in frequency renders this source of contamination to values $< 1 \mu\text{K}$ at both demodulations and in all channels. These upper limits are further reduced by the fact that our experiment probes higher values of ℓ 's than those probed by the Tenerife experiment, and at high $|b|$ the Galactic power spectrum scales as $C_\ell \propto \ell^{-3}$ (Tegmark & Efstathiou 1996; Kogut *et al.* 1996a; Gautier *et al.* 1992).

The presence of atmospheric residuals is also tested by allowing for the presence of a signal with a spectral index in antenna temperature of $n = 0., 0.2$ and 0.4 . The $n = 0$ case corresponds to the approximate case in which the effective atmospheric temperature is the same in all our channels. The $n = 0.2$ and 0.4 cases allow an increase with frequency of the effective atmospheric temperature. For all the considered n values, the likelihood assigns the bulk of the fluctuations to CMB signal: $C_{0,cmb}^{1/2} = 72_{-24}^{+26} \mu\text{K}$, $C_{0,atm}^{1/2} < 20 \mu\text{K}$. As shown in table 9, these values are rather insensitive to the exact choice of the spectral index n .

The two-component joint likelihood analysis on the 1F data places the bulk of the

signal on the atmospheric component: $C_{0,atm}^{1/2} = 189_{-39}^{+54} \mu\text{K}$ and $C_{0,cmb}^{1/2} = 159_{-63}^{+69} \mu\text{K}$, which in flat band power estimate becomes $\sqrt{\bar{\ell}(\bar{\ell} + 1)C_{\bar{\ell}}/(2\pi)} = 4.1_{-1.6}^{+1.8} \cdot 10^{-5}$. Treating the calibration uncertainty as a systematic effect, the above results for the CMB component become : $C_{0,cmb}^{1/2} = 159_{-87}^{+93} \mu\text{K}$ and $\sqrt{\bar{\ell}(\bar{\ell} + 1)C_{\bar{\ell}}/(2\pi)} = 4.1_{-2.1}^{+2.4} \cdot 10^{-5}$. Having a large atmospheric signal in our 1F data is expected because the 1F demodulation is known to be less efficient in removing linear gradients in the atmospheric signal. However, a significant fraction of the signal is projected to the CMB component which is marginally consistent with the 2F result. When testing for the presence of Galactic contamination the two-component likelihood analyses yield low significance detection for a dust component, and only upper limits to contamination by free-free or synchrotron emission.

8. CONCLUSIONS

This work demonstrates that it is possible to achieve sensitivities of a few tens of μK in the study of CMB temperature anisotropy at millimetric wavelengths from ground based observatories. This requires sites with stable and dry atmosphere and the combination of long observing periods, measurements at several frequencies and a careful subtraction of the atmospheric contribution. Other conclusions of this work are:

1. The sensitivity achieved in the 2F demodulation allows us to identify a common signal between our channels with a value of $C_0^{1/2} = 72_{-24}^{+26} \mu\text{K}$ corresponding to a band power estimate of $\sqrt{\bar{\ell}(\bar{\ell} + 1)C_{\bar{\ell}}/(2\pi)} = 2.0_{-0.8}^{+1.0} \cdot 10^{-5}$ at $\bar{\ell} = 53_{-15}^{+22}$ at 68% CL including the systematic effect due to calibration uncertainty. We believe calibration uncertainty should be treated as a systematic error and not added in quadrature to the error bar.
2. Our value is consistent with the detection reported by the Saskatoon experiment at the same angular scale.

3. Two alternative arguments (one based on extrapolations from Galactic templates, the other on results from other experiments) allow us to discard a Galactic origin of the detected signal. An extension of the likelihood analysis allowing the presence of a signal with the assumed spectrum for the atmospheric emission also discards the possibility of the signal being caused by correlated atmospheric residuals.
4. We have used a simple technique for reducing the atmospheric noise in millimetric observations. We have presented tests on the performance of this technique by looking at the power spectra of the data before and after applying it. The reduction of the noise is also observed by comparing the distribution of the noise before and after cleaning the data.
5. We have detected the Galactic Plane crossing in all cleaned channels at both demodulations. This constitutes the best check of the performance of the technique.
6. In all channels the 1F data show an excess of signal with respect to the 2F data. This excess is suspected to be of atmospheric origin. The two-component joint likelihood analysis assigns a portion of the detected signal to CMB fluctuations at a level of $C_0^{1/2} = 159_{-87}^{+93} \mu\text{K}$ or in band power estimate $\sqrt{\bar{\ell}(\bar{\ell} + 1)C_{\bar{\ell}}/(2\pi)} = 4.1_{-2.1}^{+2.4} \cdot 10^{-5}$ at 68% CL including calibration uncertainty as a systematic effect. Our detected signal in the 1F demodulation corresponds to an ℓ -range never before observed.

We expect to improve the results presented in this work with the addition of the new data taken during the Spring of 1996.

This work has been supported by a University of Delaware Research Foundation (UDRF) grant, by the Bartol Research Institute and the Spanish DGICYT project PB 92-0434-c02 at the Instituto de Astrofísica de Canarias. We want to thank L. Page and

S. Meyer for considerable help in all the phases of this project. A special thank for the support of L. Shulman, J. Poirer, R. Hoyland and the technical staff of the Observatorio del Teide. Special thanks to B. Keating for his careful reading of the manuscript. Finally we would like to thank the staff from the Instituto Nacional de Meteorología at Tenerife who very kindly provided us with the atmospheric data used in this analysis and to R.A. Watson for his help in the use of these data.

REFERENCES

- Andreani P., *et al.* , 1991, A. & A., 249, 299
- Banday, A.,J. & Wolfendale,A.,W., 1991, MNRAS, 252,462
- Barkat, M., 1991, Signal: Detection & Estimation (London: Artech House)
- Bennett, C. L., *et al.* 1992, ApJ, 391, 466
- Bennett, C. L., *et al.* 1992, ApJ, 396, L7
- Bennett, C.L. *et al.* , 1996, ApJ, 464, L1
- Bersanelli, M., *et al.* 1995, ESA Rep. D/SCI(96)3
- Boulanger, F., Abergel, A., Bernard, J.-P., Burton, W.B., Désert, F.-X., Hartmann, D.,
Lagache, G., & Puget, J.-L., 1996, A&A, 312, 256
- Cernicharo, J., 1985, IRAM Internal Report,52
- Church, S.E., *et al.* 1997, ApJ, 484, 523
- Condon,J.J, Broderick,J.J & Seielstad,G.A. 1989, AJ, 97, 1064
- Davies, R.D., Gutiérrez, C.M., Hopkins, J., Melhuish, S.J., Watson, R.A., Hoyland, R.J.,
Rebolo, R., Lasenby & Hancock, S.,1996, MNRAS, 278, 883
- de Bernardis,P., Masi, S. & Vittorio, N. , 1991, ApJ, 382, 515
- Fischer, M. L., Clapp, A., Devlin, M., Gundersen, J.O., Lange, A.E., Lubin, P.M., Meinhold,
P.R., Richards, P.L. & Smoot, G.F., 1995, ApJ, 226
- Franceschini, A., Toffolatti, L., Danese, L., & De Zotti, G. 1989, ApJ, 344, 35
- Ganga, K., Cheng, E., Meyer, S., & Page, L., 1993, ApJ, 410, L57

- Gautier, T. N., Boulanger, F., Perault, M. & Puget, J. L., 1992, AJ, 102, 1313
- Gundersen, J. O., *et al.* 1995, Ap. J. , 443, L57
- Gutiérrez, C. M., 1997, ApJ, 483, 51
- Gutiérrez, C. M., Hancock, S., Davies, R. D., Rebolo, R., Watson, R. A., Hoyland, R. J.,
Lasenby, A. N., & Jones, A. W., 1997, Ap. J. , 480, 83
- Hagfors, T., 1970, Radio Science, 5, 189
- Hancock, S., *et al.* , 1994, Nature, 367, 333
- Hancock, S., *et al.* , 1997, MNRAS, in press.
- Hancock, S., *et al.* , 1997, MNRAS, in press.
- Haslam, C. G. T., *et al.* 1982, AAS ,47,1
- Kogut, A., *et al.* 1996, ApJ, 460, 1
- Kogut, A., *et al.* 1996, Ap. J. , 464, L5
- Kühr, H., Witzel, A., Pauliny-Toth, I.I.K. & Nauber, U. 1981, A&AS, 45, 367
- Netterfield, C. B., Devlin, M. J., Jarolik, N.; Page, L. & Wollack, E. J., 1997, ApJ,474, 47
- Page, L.,A., Cheng, S. & Meyer, S., S., Ap. J. , 355,L1
- Piccirillo L., 1991, Rev. Sci. Instr., 62, 1293
- Piccirillo L. & Calisse P., 1993, ApJ, 411, 529
- Piccirillo, L., Femenía, B., Kachwala, N., Rebolo, R., Limon, M., Gutiérrez, C. M., Nicholas,
J., Schaefer, R. K. & Watson, R. A., 1997, Ap. J. , 475, L77

Platt, S. R., Kovac, J., Peterson, J.B., & Ruhl, J. E., 1997, *Ap. J.* , 475, L1

Reach, W. T. *et al.* , 1995, *ApJ*, 451, 188

Reich, P. & Reich, W., 1986, *A&A*, 63,205

Scott, P.F., Saunders, R., Pooley, G., O’Sullivan, C., Lasenby, A.N., Jones, M., Hobson, M.P., Duffett-Smith, P.J. & Baker, J., 1996, *Ap. J.* , 461, L1

Steinhardt, P.J.,in *Proc. CWRU Conf. on the CMB, CMB COBE: Anisotropies Two Years After Observations, Theory, and the Future*, ed. L. Krauss (Singapore: COBE: World Scientific)

Tegmark, M. & Efstathiou, G., 1996, *MNRAS*, 281, 1297

White, M. & Srednicki, M., 1995, *ApJ*, 443, 6

Wright *et al.* , 1991, *ApJ*, 381, 200

Fig. 1.— Window function for the 1F and 2F demodulations at angular separation $\psi = 0$.

Fig. 2.— Astronomical calibration by observing the Moon at the 1F demodulation. Solid lines are the data and dashed lines the predictions using the Lunar models cited in text.

Fig. 3.— Meteorological conditions during the 1994 observing campaign.

Fig. 4.— Power spectra of the in- and out-phase components at both demodulations and for all channels for a typical night of observation. Temperatures in this figure refer to antenna temperature values.

Fig. 5.— Distribution of *rms* values for the whole campaign before applying the cleaning technique for the 1F (solid line) and 2F (dash-dot line) demodulations. Note the height of the last bin in each histogram, as it contains the contributions of that bin plus all following bins. Temperatures in this figure refer to thermodynamic temperature values.

Fig. 6.— Mean auto-correlation curves for all channels and both demodulations of the raw data. Dotted lines represent the $\pm 1\sigma$ limits.

Fig. 7.— The different stages of the cleaning technique. Panels in the left column show the raw data. Center panels display the output of equation (3), superimposed the sinusoidal fit (thick dashed line). Right panels show the cleaned data with the baseline removed. All plots have been brought to a bin size of 3° in RA for display purposes. Temperatures in this figure refer to thermodynamic temperature values.

Fig. 8.— Final data sets in the regions to be considered for the posterior Likelihood analysis. The data have been binned to 3° in RA for clarity. We show the 1F and 2F profiles indicating the instrument response to point sources. Temperatures in this figure refer to thermodynamic temperature values.

Fig. 9.— Power spectra of a typical night of observation in thermodynamic temperature at 10s before (thin line) and after (bold line) applying the cleaning technique. The dashed lines represent the upper limits to the instrument noise as estimated in section 4.1. Temperatures are expressed in thermodynamic units.

Fig. 10.— Distribution of *rms* values after cleaning and editing for all the observing nights eligible to be cleaned. Notice the height of the last bin in each histogram for it contains the contributions of that bin plus all following bins. Temperatures in this figure refer to thermodynamic temperature values.

Fig. 11.— Comparison of the recovered Galactic Plane crossings at channels 1, 2 and 3 and at both demodulations with the predictions in thermodynamic temperature.

Fig. 12.— Mean cross-correlation curves between overlapping sections of individual nights used to generate the final data sets at any two channels.

Fig. 13.— Contour plots of the likelihood surface of the joint analysis on channels 1,2 and 3 for the 1F demodulation when a second component other than CMB is allowed. The four indeces represent the four relevant foregrounds: dust, atmosphere,free-free and synchrotron emission. Contour levels represent the confidence levels at 68% (solid line) and 95% (dashed line). The X symbol indicates the position of the likelihood surface peak. Temperatures on the axis are in thermodynamic units.

Fig. 14.— Contour plots of the likelihood surface of the joint analysis on channels 1,2 and 3 for the 1F demodulation when a second component other than CMB is allowed. The four indeces represent the four relevant foregrounds: dust, atmosphere,free-free and synchrotron emission. Contour levels represent the confidence levels at 68% (solid line) and 95% (dashed line). The X symbol indicates the position of the likelihood surface peak. Temperatures on the axis are in thermodynamic units.

Table 1. Results From Fits To Extended Moon Transits.

	1F DEMODULATION		2F DEMODULATION	
	σ	β_0	σ	β_0
Ch 1	0.94 ± 0.10	2.89 ± 0.09	1.01 ± 0.27	2.80 ± 0.29
Ch 2	0.88 ± 0.07	2.90 ± 0.06	0.92 ± 0.19	2.85 ± 0.19
Ch 3	0.85 ± 0.06	2.90 ± 0.05	0.88 ± 0.17	2.86 ± 0.16
Ch 4	0.82 ± 0.07	2.91 ± 0.06	0.84 ± 0.13	2.88 ± 0.13

Table 2. Correlation Between Channels Before Applying Atmospheric Correction.

	1F DEMODULATION		2F DEMODULATION	
	Whole Campaign	Final Data Set	Whole Campaign	Final Data Set
Ch 1 - Ch 4	0.965 ± 0.010	0.990 ± 0.010	0.884 ± 0.023	0.91 ± 0.09
Ch 2 - Ch 4	0.983 ± 0.008	0.995 ± 0.011	0.977 ± 0.007	0.991 ± 0.010
Ch 3 - Ch 4	0.99963 ± 0.00010	0.99984 ± 0.00010	0.9956 ± 0.0011	0.995 ± 0.010

Table 3. Data Used To Generate Final Data Sets.

1F DEMODULATION				
	Percentage	Number nights	Mean <i>rms</i> (mK)	Amplitude Baseline (mK)
Ch 1	17.2 %	16	0.392 ± 0.024	0.78 ± 0.19
Ch 2	13.3 %	14	0.48 ± 0.07	1.23 ± 0.23
Ch 3	16.8 %	12	1.30 ± 0.14	1.81 ± 0.23
2F DEMODULATION				
Ch 1	30.1 %	24	0.275 ± 0.024	0.46 ± 0.08
Ch 2	15.4 %	18	0.233 ± 0.018	0.85 ± 0.23
Ch 3	14.5 %	15	0.86 ± 0.12	1.28 ± 0.25

Note. — Mean *rms* and baseline amplitudes are expressed in thermodynamic units.

Table 4. Noise Spectrum ($mK s^{1/2}$) Before And After Applying Atmospheric Subtraction.

Channel	1F Out	1F Out	1F In	1F In	2F Out	2F Out	2F In	2F In
	1 Hz	0.001 Hz	0.001 Hz	0.001 Hz	1 Hz	0.001 Hz	0.001 Hz	0.001 Hz
	CLEANED				CLEANED			
1	4.8±0.4	6.9±0.6	52±5	8.1±1.0	3.6±0.3	6.7±0.6	8.8±0.7	6.1±0.7
2	1.13±0.10	1.87±0.17	115±10	3.9±0.5	1.04±0.11	3.5±0.4	12.3±1.1	3.3±0.4
3	1.99±0.18	3.6±0.3	570±50	20.0±2.3	1.81±0.17	16.0±1.5	55±5	12.7±1.5
4	1.20±0.11	18.9±1.7	750±60	...	1.07±0.10	27.6±2.6	94±8	...

Note. — Mean *rms* and baseline amplitudes are expressed in thermodynamic units.

Table 5. Values Of ρ_{i4} For The Models Under Consideration.

Model	Reference	1F DEMODULATION			2F DEMODULATION		
		ρ_{14}	ρ_{24}	ρ_{34}	ρ_{14}	ρ_{24}	ρ_{34}
1	1	0.1167	0.1515	0.6458	0.1567	0.1533	0.6452
2	1	0.1249	0.1533	0.6453	0.1750	0.1551	0.6446
3	3	0.1292	0.1786	0.6724	0.1458	0.1787	0.6720
4	3	0.1291	0.1720	0.6624	0.1505	0.1720	0.6618
5	4	0.1233	0.1528	0.6454	0.1725	0.1546	0.6448
6	5	0.1229	0.1859	0.6778	0.1273	0.1851	0.6775
7	6	0.1147	0.1555	0.6511	0.1397	0.1556	0.6506
8	7	0.1137	0.1780	0.6739	0.1178	0.1773	0.6736
9	8	0.1195	0.1788	0.6723	0.1269	0.1779	0.6719
10	9	0.1386	0.2229	0.7063	0.1379	0.2224	0.7061
11	10	0.1552	0.1654	0.6438	0.1678	0.2105	0.6427
12	11	0.1299	0.1748	0.6649	0.1464	0.1749	0.6644

References. — (1) Boulanger *et al.* 1996; (2) Reach *et al.* 1995; (3) Wright *et al.* 1991; (4) Bersanelli *et al.* 1995; (5) Davies *et al.* 1996a; (6) Kogut *et al.* 1996a; (7) Kogut *et al.* 1996b; (8) de Bernardis *et al.* 1991; (9) Banday & Wolfendale 1991; (10) Page *et al.* 1990; (11) Fischer *et al.* 1995.

Table 6. Expected *rms* Values Due To Diffuse Galactic Emission. Units Of μK .

Model	Reference	Description	1F DEMODULATION			2F DEMODULATION		
			<i>rms_{Ch1}</i>	<i>rms_{Ch2}</i>	<i>rms_{Ch3}</i>	<i>rms_{Ch1}</i>	<i>rms_{Ch2}</i>	<i>rms_{Ch3}</i>
1	1	$I_\nu^D \propto \nu^2 B_\nu(17.5)$	1.2	2.4	12.3	0.6	1.3	6.7
2	1	$I_\nu^D \propto \nu^2 B_\nu(18.2)$	1.1	2.2	11.3	0.6	1.2	6.1
3	2	$I_\nu^D \propto \nu^2 (B_\nu(20.4) + 6.7 \times B_\nu(4.8))$	1.5	3.1	13.6	0.8	1.7	7.4
4	3	$I_\nu^D \propto \nu^{1.65} B_\nu(23.2)$	1.5	2.9	13.1	0.8	1.6	7.1
5	4	$I_\nu^D \propto \nu^2 B_\nu(18.0)$	1.1	2.3	11.6	0.6	1.2	6.3
6	5	$I_\nu^D \propto \nu^{1.4} B_\nu(23.3)$	2.5	4.9	19.6	1.3	2.6	10.6
7	6	$I_\nu^D \propto \nu^{1.9} B_\nu(18)$	1.3	2.8	13.7	0.7	1.5	7.4
8	7	$I_\nu^D \propto \nu^{1.5} B_\nu(20)$	2.5	5.2	21.4	1.3	2.8	11.6
9	8	$I_\nu^D \propto \nu^{1.5} B_\nu(22)$	2.2	4.3	18.2	1.1	2.3	9.8
10	9	$I_\nu^D \propto \nu B_\nu(22.1)$	7.0	12.5	41.0	3.8	6.8	22.2
11	10	$I_\nu^D \propto \nu^2 B_\nu(22.1)$	0.9	1.5	8.0	0.5	0.8	4.3
12	11	$I_\nu^D \propto \nu^{1.6} B_\nu(24)$	1.6	3.1	13.5	0.8	1.6	7.3

References. — (1) Boulanger *et al.* 1996; (2) Reach *et al.* 1995; (3) Wright *et al.* 1991; (4) Bersanelli *et al.* 1995; (5) Davies *et al.* 1996a; (6) Kogut *et al.* 1996a; (7) Kogut *et al.* 1996b; (8) de Bernardis *et al.* 1991; (9) Banday & Wolfendale 1991; (10) Page *et al.* 1990; (11) Fischer *et al.* 1995.

Note. — I_ν^D and $B_\nu(T)$ stand for the dust spectrum and a black-body spectrum at a temperature of T Kelvin, respectively. Models (3) and (4) differ in the dust spectrum at low $|b|$.

Table 7. Basic Statistic Figures Of Final Data Sets.

	RA_1				RA_2			
	Range ($^{\circ}$)	Mean # points	Mean σ (μK)	Mean rms (μK)	Range ($^{\circ}$)	Mean # points	Mean σ (μK)	Mean rms (μK)
Ch 1 1F	[224,285]	7.9	130.6	134.3	[331,369]	10.8	103.1	123.7
Ch 2 1F	[230,285]	8.3	118.9	157.9	[331,361]	7.4	113.2	110.6
Ch 3 1F	[224,285]	8.8	312.6	340.5	[331,367]	8.7	310.6	443.6
Ch 1 2F	[206,285]	12.6	74.7	62.5	[331,381]	13.2	74.1	74.4
Ch 2 2F	[229,285]	9.1	68.5	71.0	[331,360]	9.5	53.3	58.5
Ch 3 2F	[236,285]	8.3	236.4	197.9	[331,362]	9.5	187.7	204.7

Note. — Mean σ refers to the mean error bar associated with each in the final data set. Mean rms is the weighted rms along the indicated RA range. Both quantities expressed in thermodynamic units.

Table 8. Likelihood Results On Individual Data Sets. Values In $\mu\text{K CMB}$.

Channel	1F DEMODULATION			2F DEMODULATION		
	$(C_0)^{1/2}$	$(C_0)^{1/2}$	$(C_0)^{1/2}$	$(C_0)^{1/2}$	$(C_0)^{1/2}$	$(C_0)^{1/2}$
	RA_1	RA_2	RA_1+RA_2	RA_1	RA_2	RA_1+RA_2
Ch 1	130^{+63}_{-52}	124^{+71}_{-58}	127^{+44}_{-37}	< 123	99^{+53}_{-45}	71^{+34}_{-37}
Ch 2	\dots	155^{+83}_{-58}	155^{+83}_{-58}	91^{+47}_{-43}	132^{+77}_{-56}	106^{+37}_{-33}
Ch 3	764^{+219}_{-169}	626^{+260}_{-176}	711^{+168}_{-135}	235^{+158}_{-181}	591^{+284}_{-240}	373^{+169}_{-163}

Note. — The stated confidence intervals do not include calibration uncertainties.

Table 9. Joint Likelihood Results. Values In μK CMB.

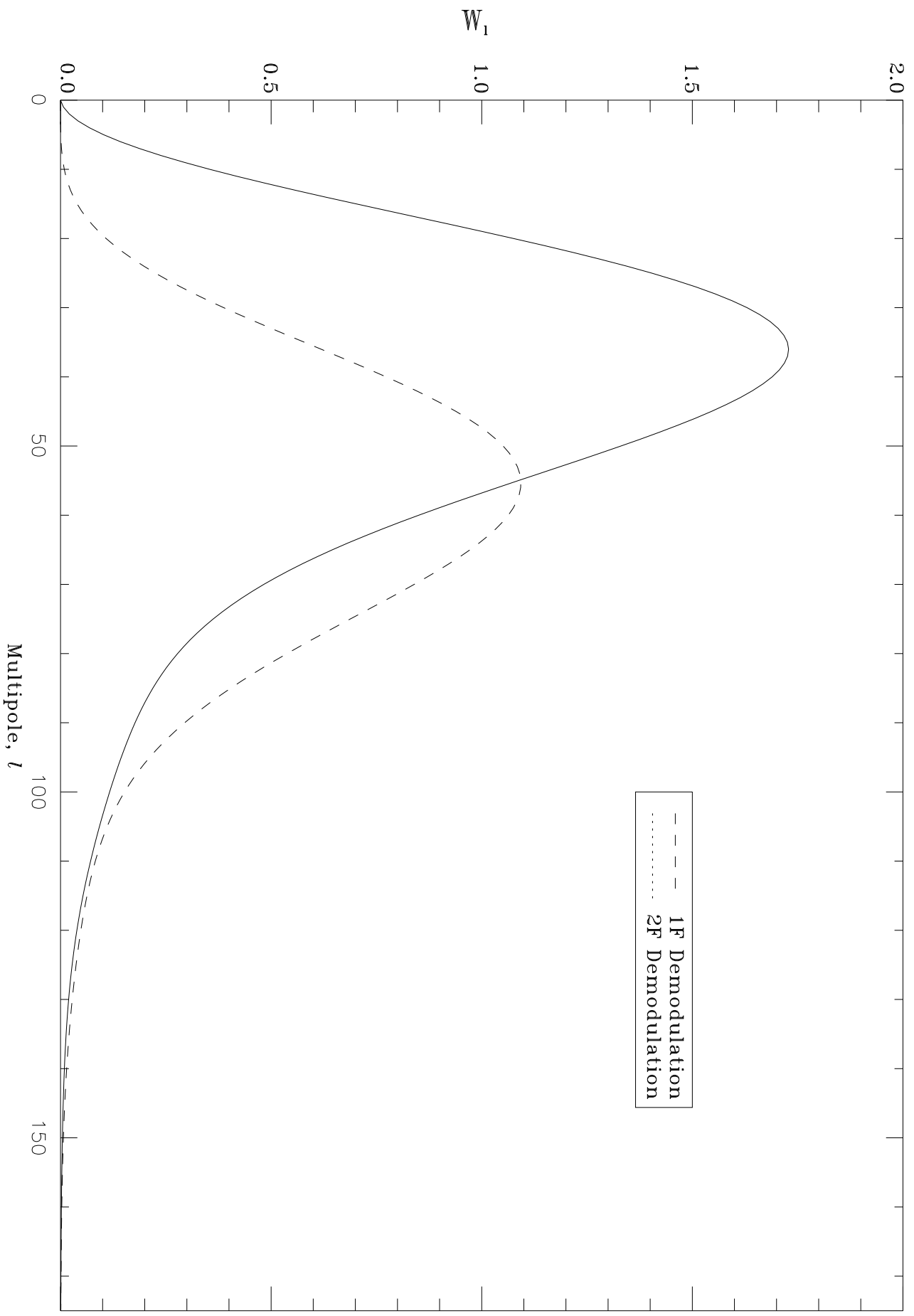
Channels	1F DEMODULATION		2F DEMODULATION	
	$(C_0)^{1/2}$ (μK)	Cross-Corr i - j	$(C_0)^{1/2}$ (μK)	Cross-Corr i - j
Ch 1 x Ch 2	129^{+41}_{-35}	0.19 ± 0.07	69^{+27}_{-25}	0.149 ± 0.026
Ch 1 x Ch 3	151^{+44}_{-37}	0.085 ± 0.013	72^{+35}_{-37}	0.049 ± 0.010
Ch 2 x Ch 3	164^{+89}_{-60}	0.31 ± 0.06	107^{+37}_{-34}	0.26 ± 0.05
Ch 1 x Ch 2 x Ch 3	150^{+40}_{-34}	...	72^{+26}_{-24}	...

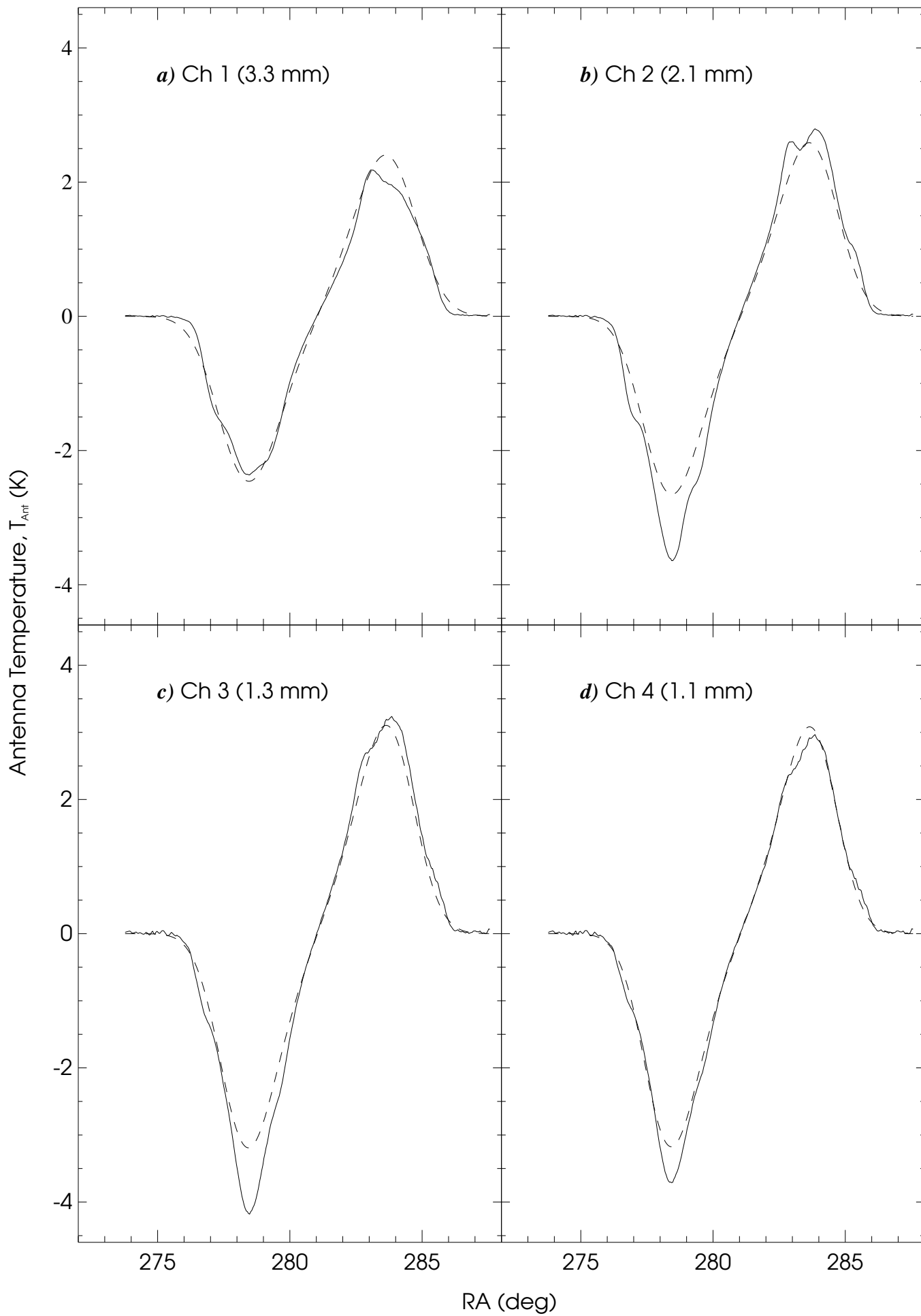
Note. — The stated confidence intervals do not include calibration uncertainties.

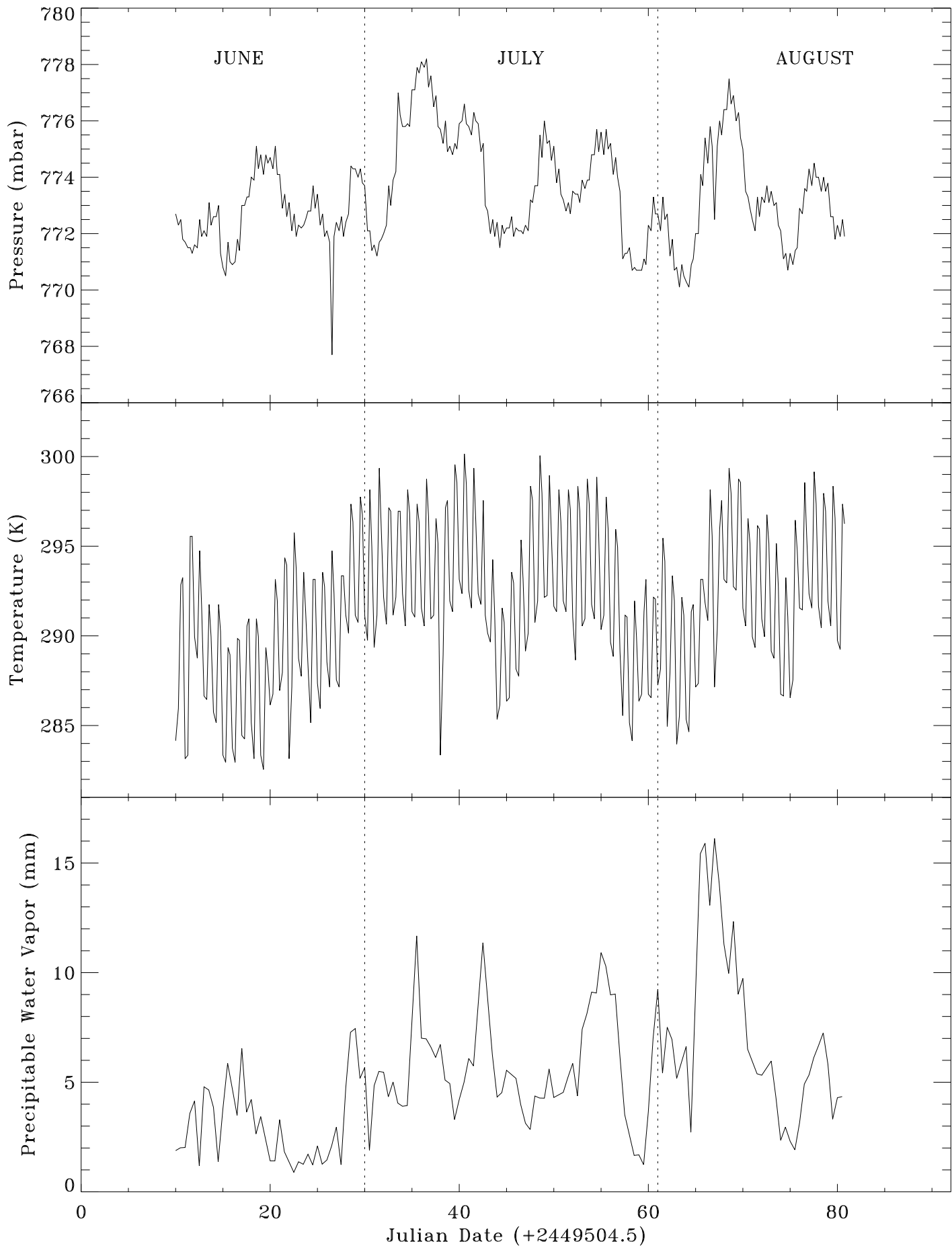
Table 10. Likelihood Results Allowing A Foreground Component. Values In $\mu\text{K CMB}$.

n	Foreground	1F DEMODULATION		2F DEMODULATION	
		$C_{0,cmb}^{1/2}$ (μK)	$C_{0,Fgd}^{1/2}$ (μK)	$C_{0,cmb}^{1/2}$ (μK)	$C_{0,Fgd}^{1/2}$ (μK)
+2.0	DUST	128_{-32}^{+42}	38_{-6}^{+8}	72_{-22}^{+26}	< 6
+1.5	DUST	128_{-34}^{+42}	60_{-10}^{+14}	72_{-22}^{+26}	< 8
+0.4	ATMOSPHERE	147_{-38}^{+54}	150_{-27}^{+39}	72_{-22}^{+26}	< 16
+0.2	ATMOSPHERE	154_{-54}^{+62}	171_{-33}^{+45}	72_{-24}^{+26}	< 18
+0.0	ATMOSPHERE	159_{-63}^{+69}	189_{-39}^{+54}	72_{-24}^{+26}	< 20
-1.8	FREE-FREE	147_{-39}^{+45}	< 177	72_{-26}^{+26}	< 62
-2.1	FREE-FREE	150_{-39}^{+45}	< 189	72_{-26}^{+26}	< 74
-2.4	FREE-FREE	153_{-39}^{+51}	< 201	72_{-26}^{+26}	< 86
-2.7	SYNCHROTRON	153_{-39}^{+51}	< 210	72_{-26}^{+26}	< 96
-3.0	SYNCHROTRON	156_{-39}^{+51}	< 216	72_{-28}^{+26}	< 106
-3.3	SYNCHROTRON	156_{-39}^{+51}	< 222	72_{-28}^{+26}	< 116

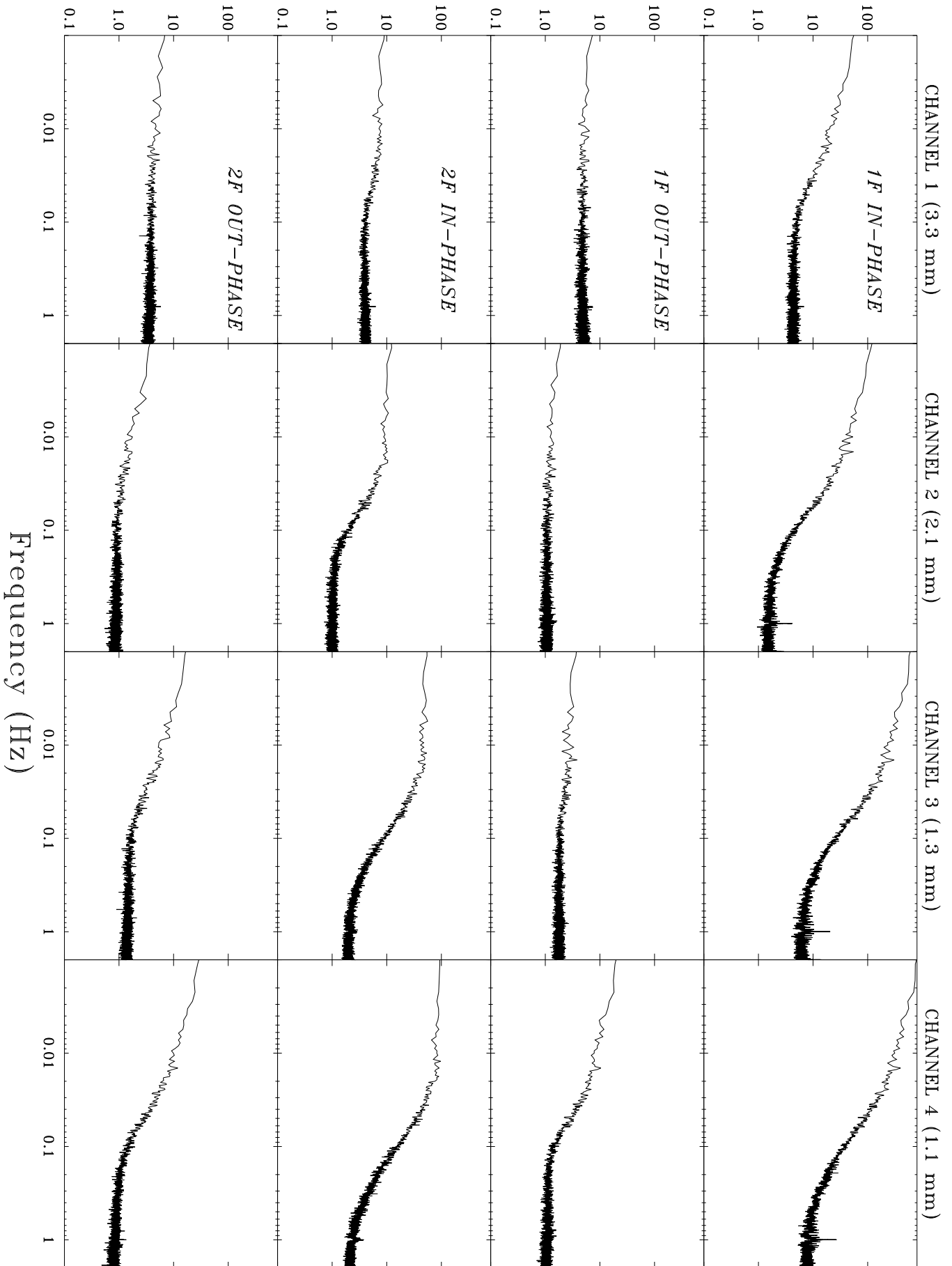
Note. — The stated confidence intervals do not include calibration uncertainties.



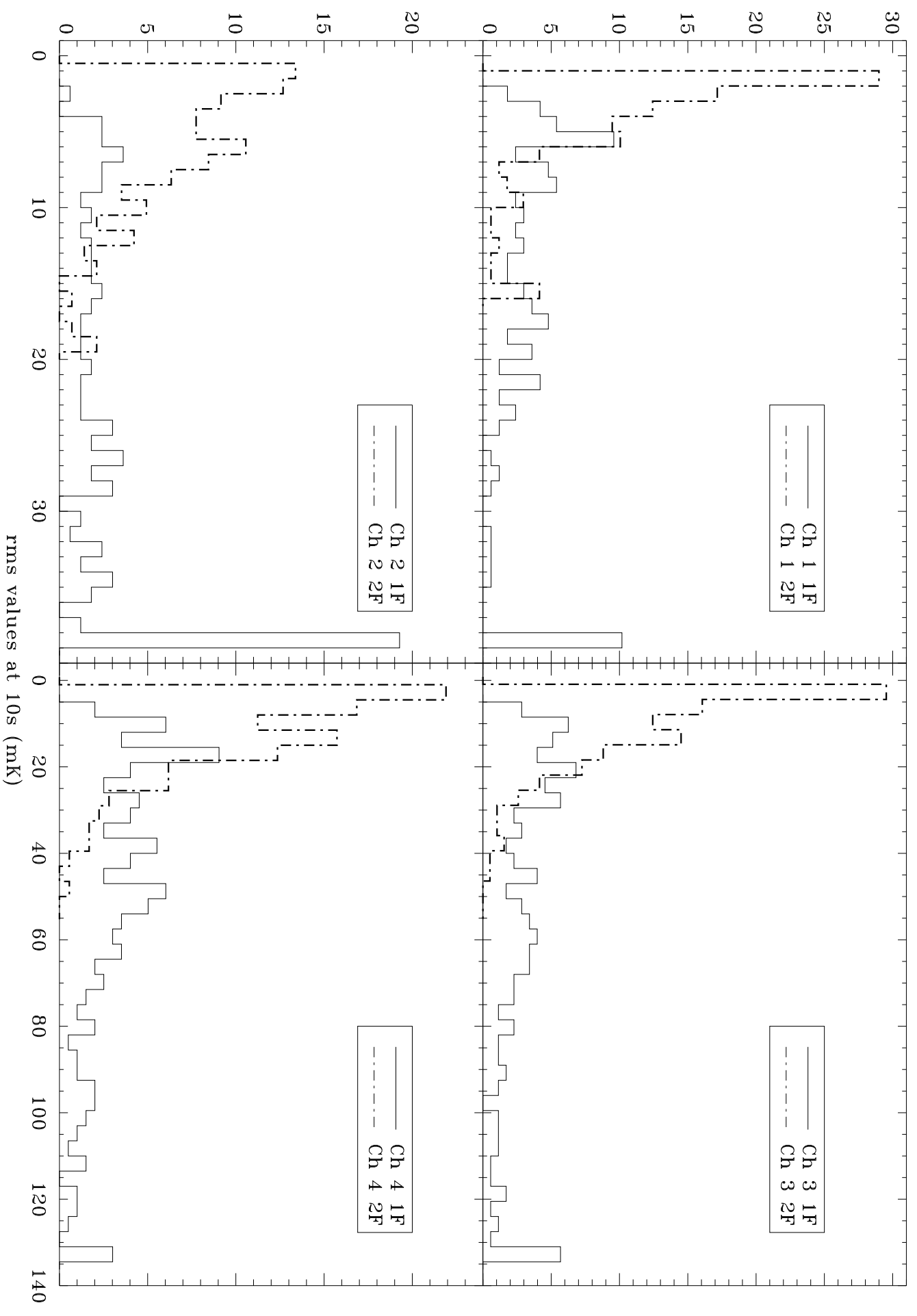




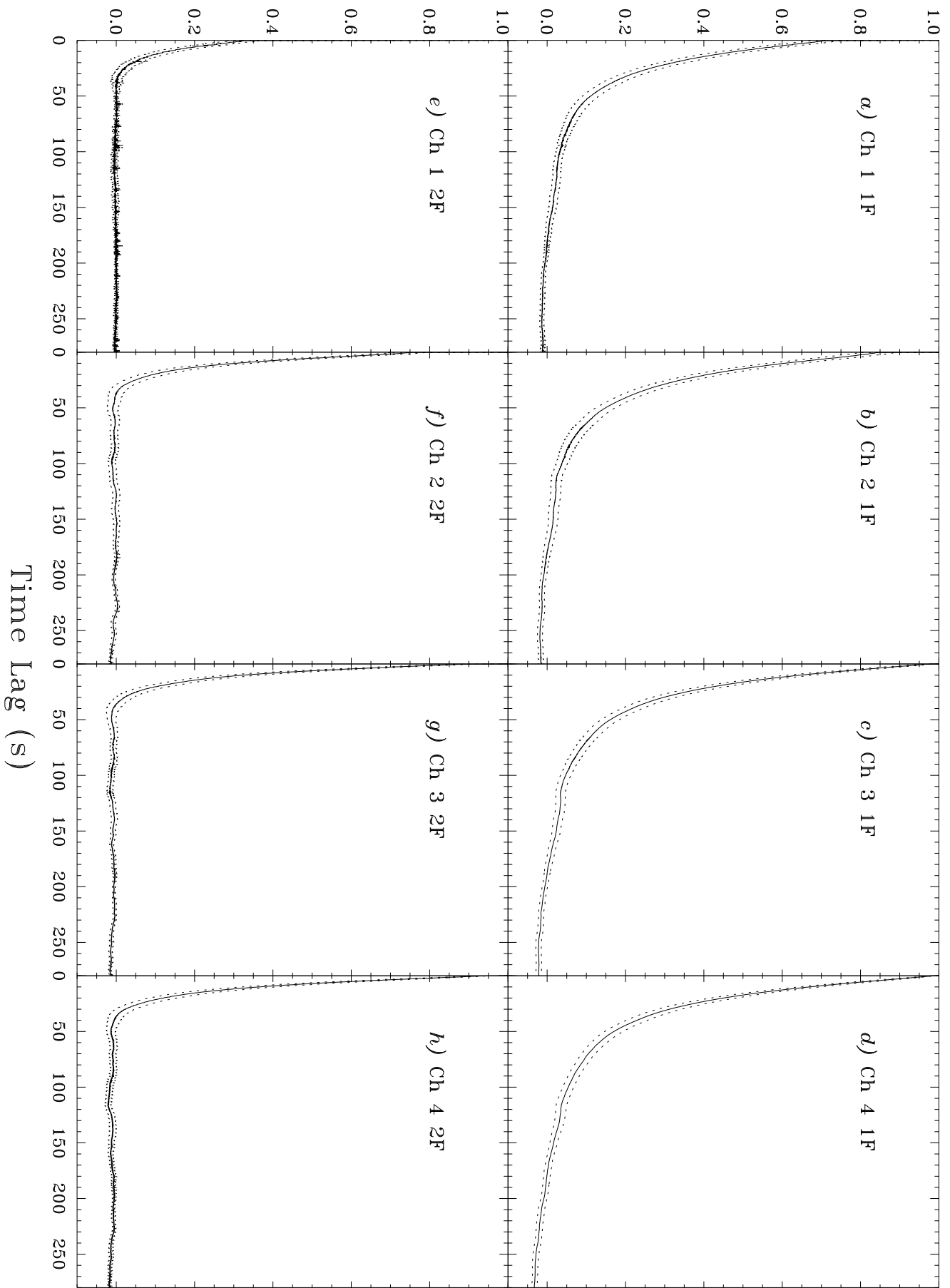
Noise Spectrum ($\text{mK s}^{1/2}$)



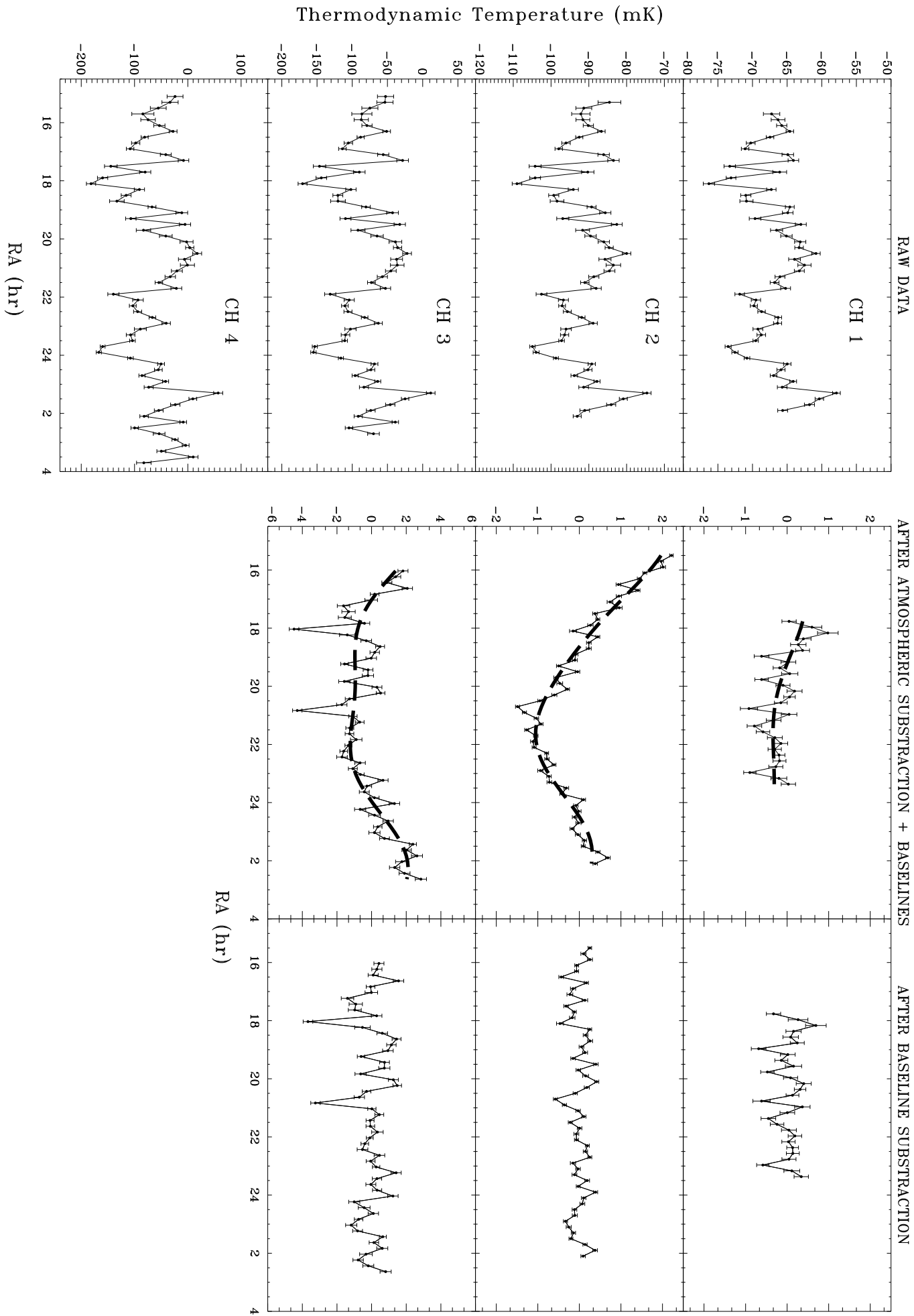
Histogram in percentage



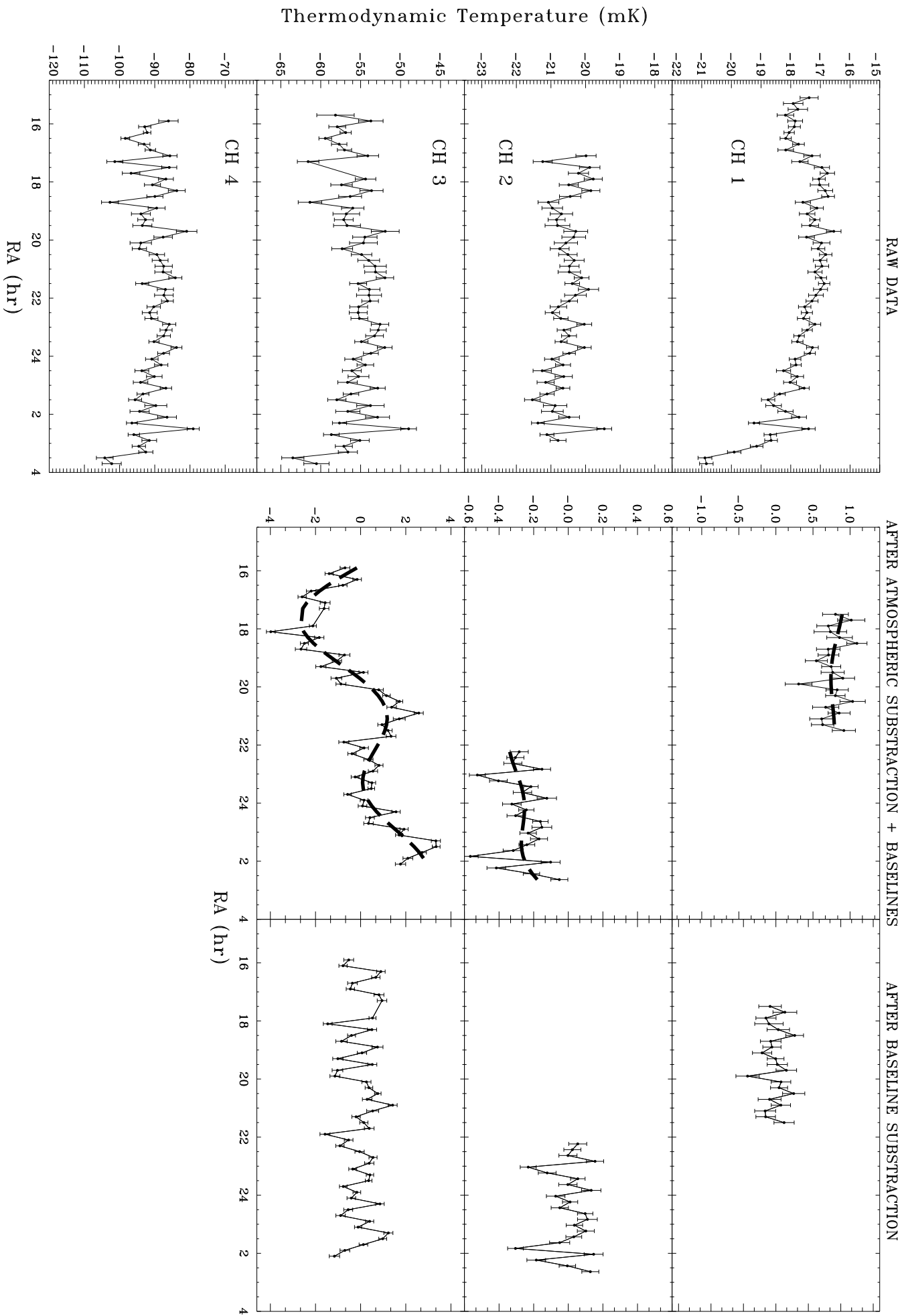
Auto-Correlation Function

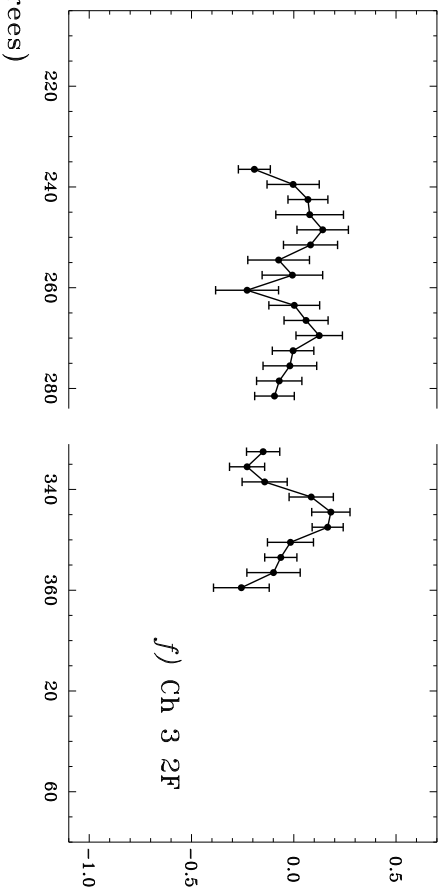
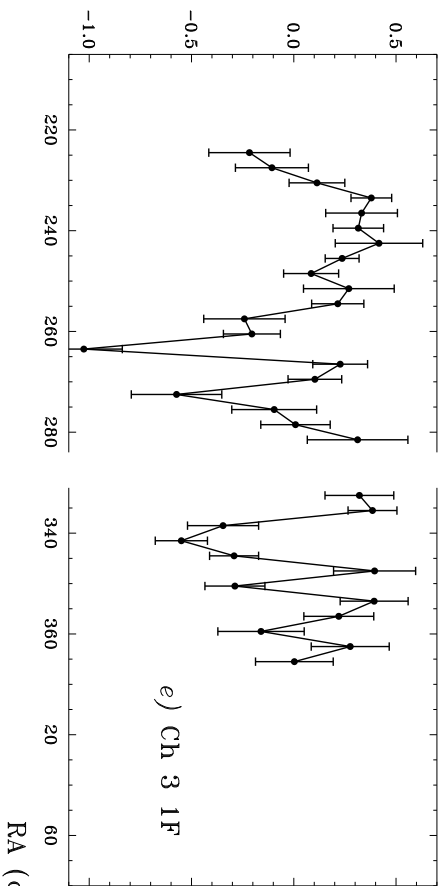
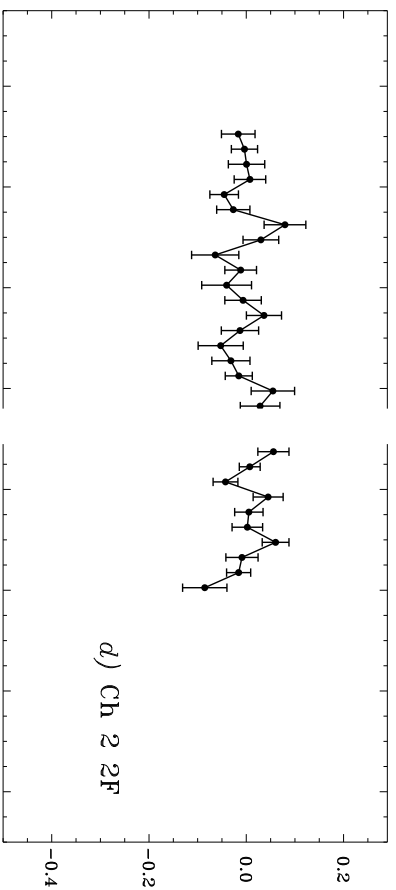
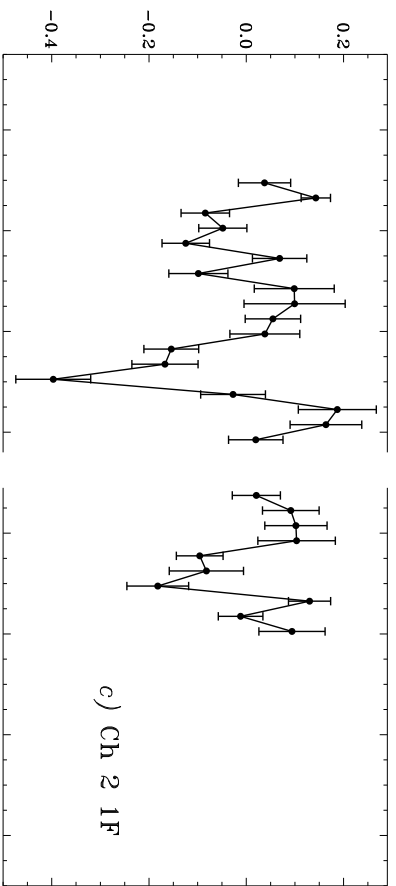
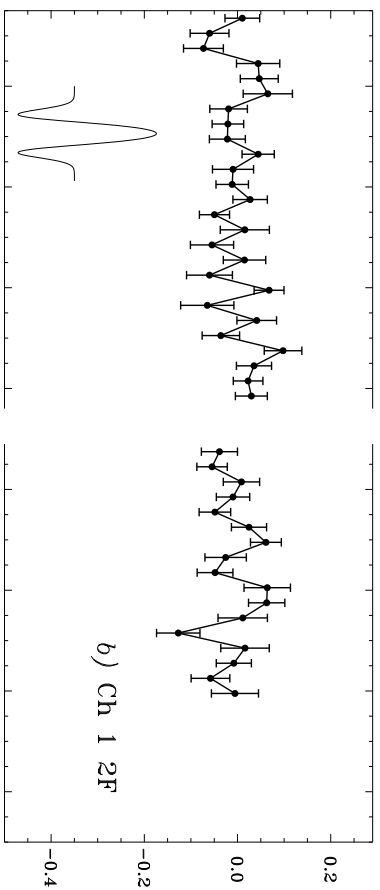
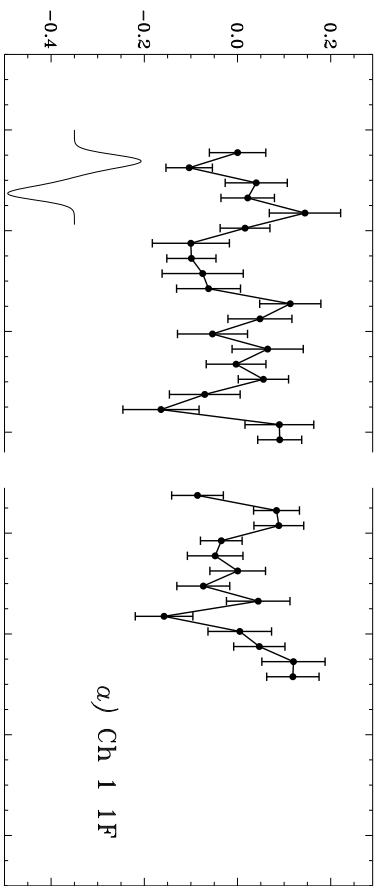


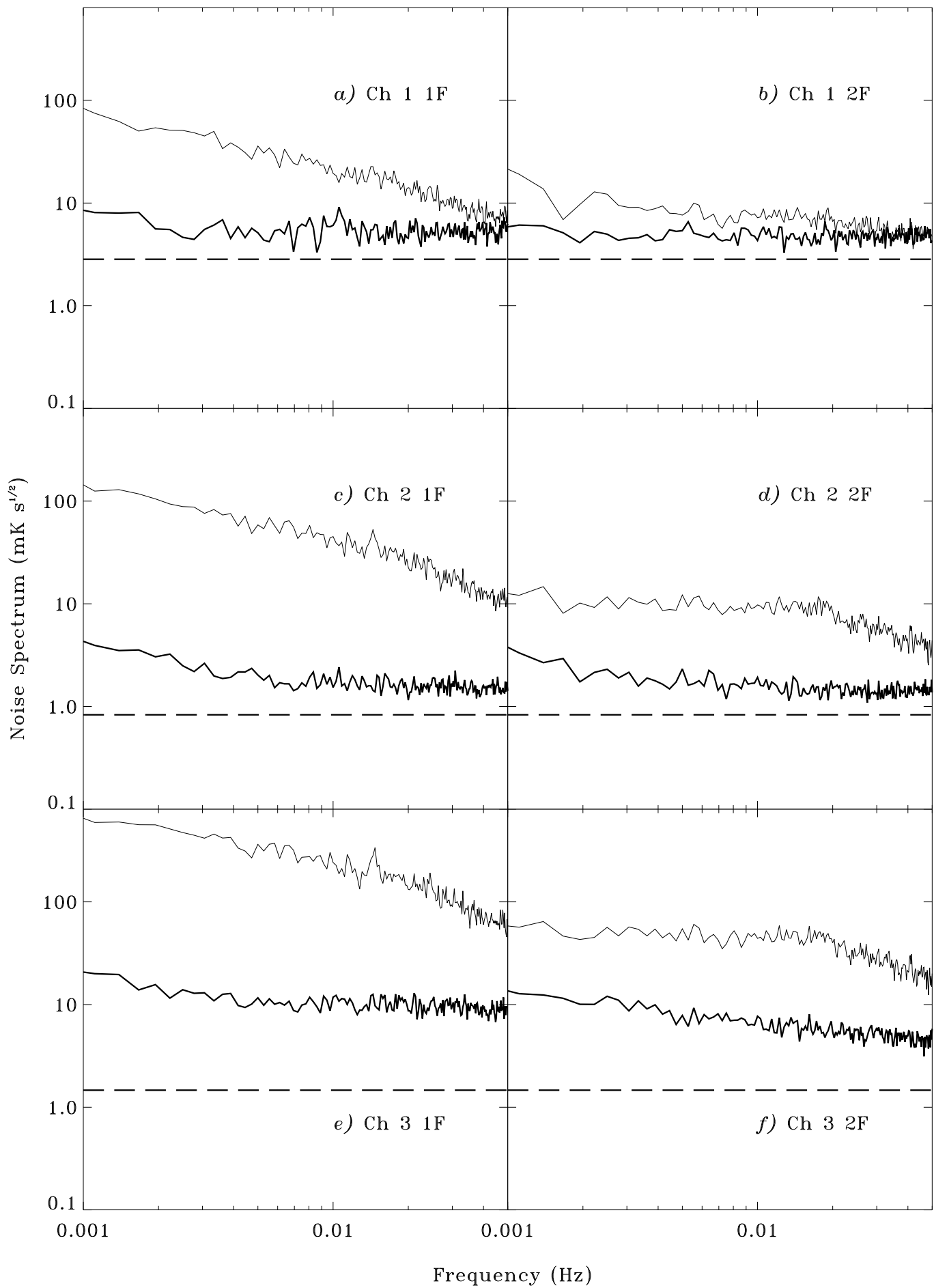
1F DEMODULATION



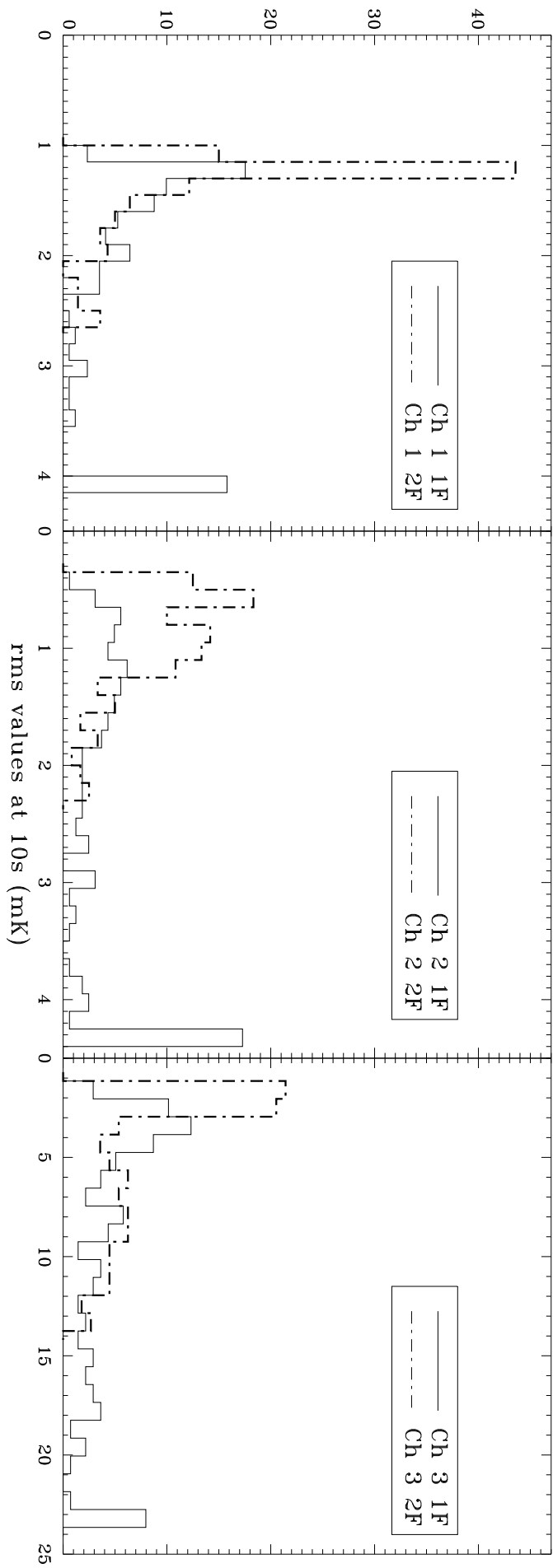
2F DEMODULATION

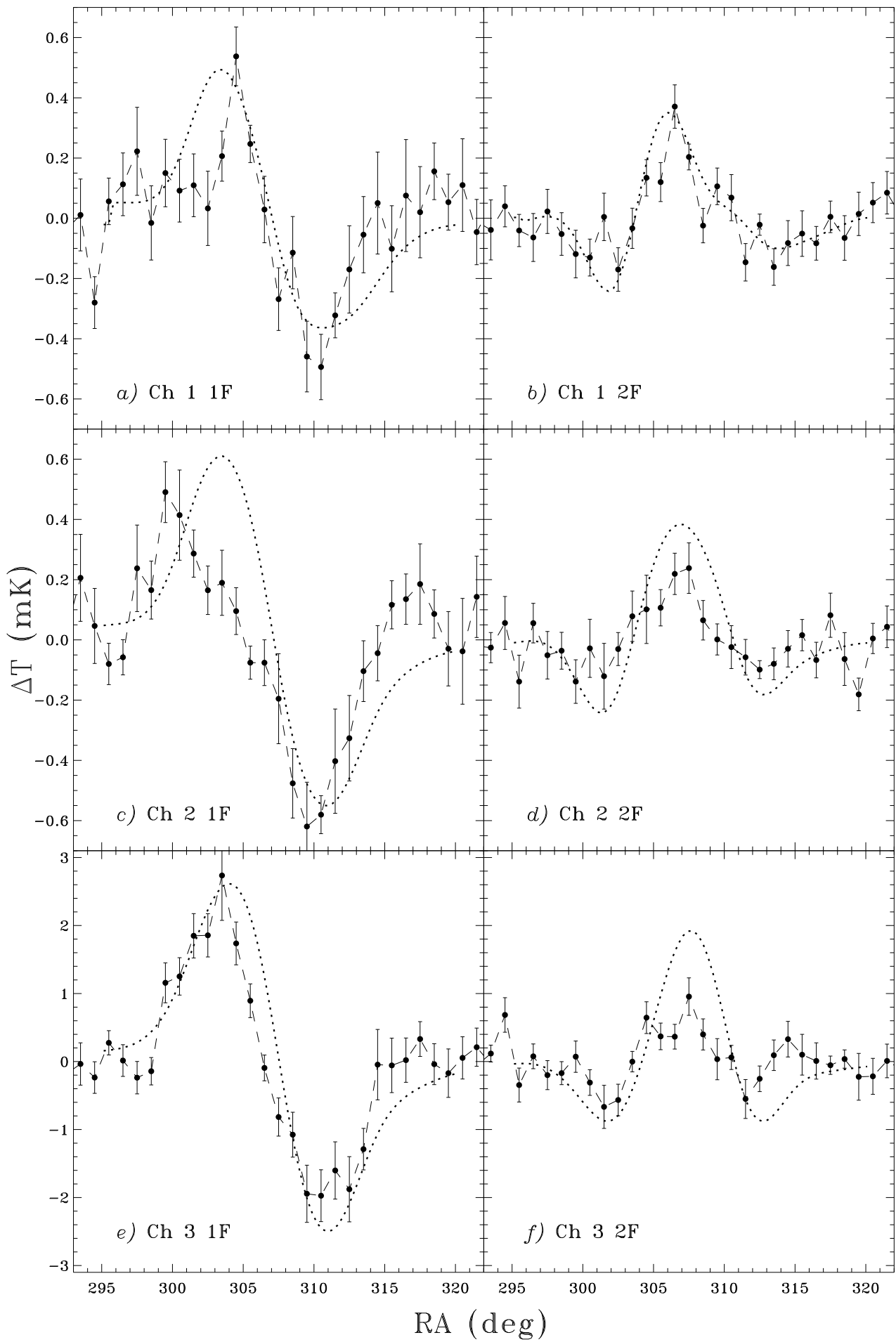


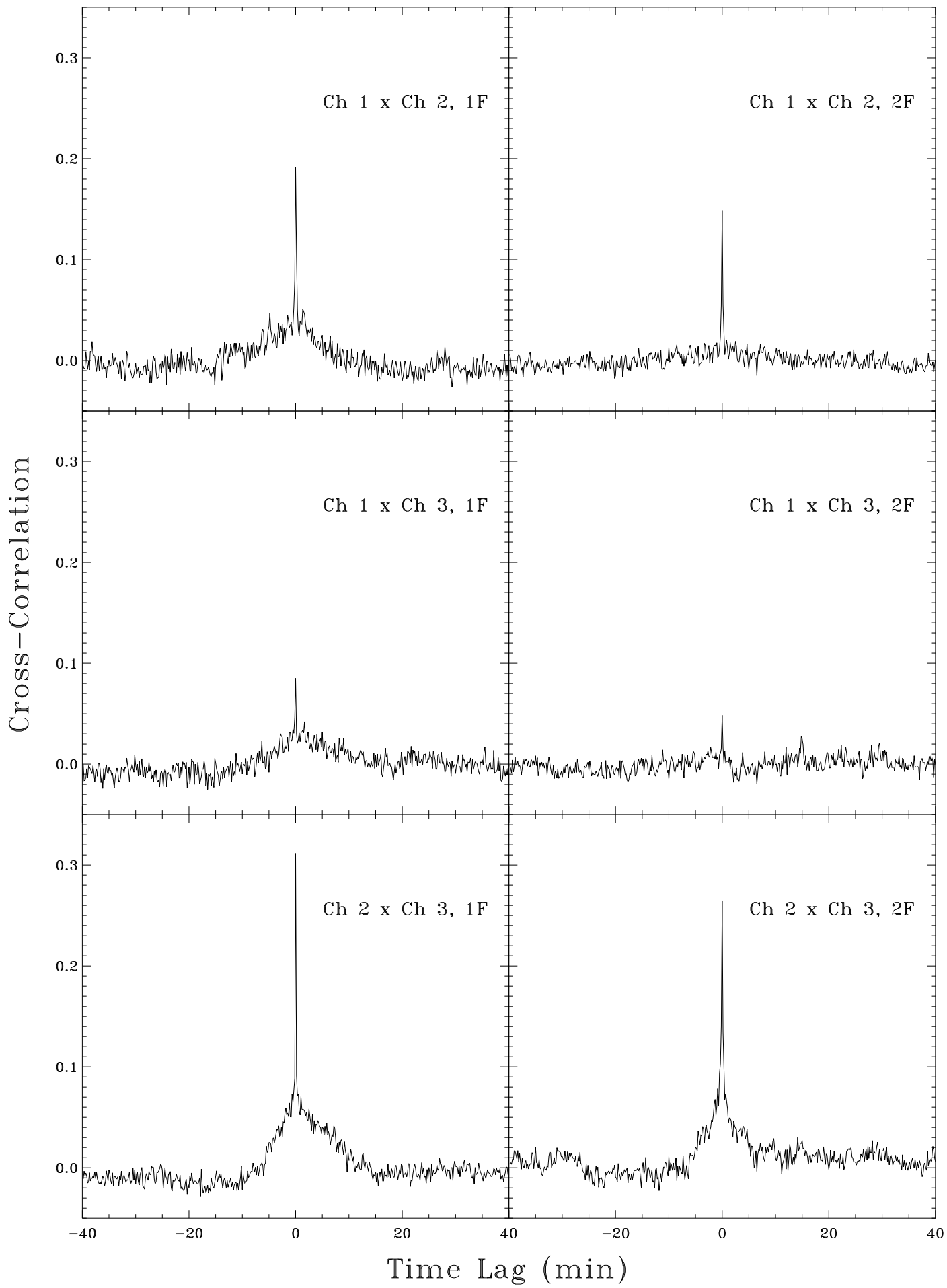


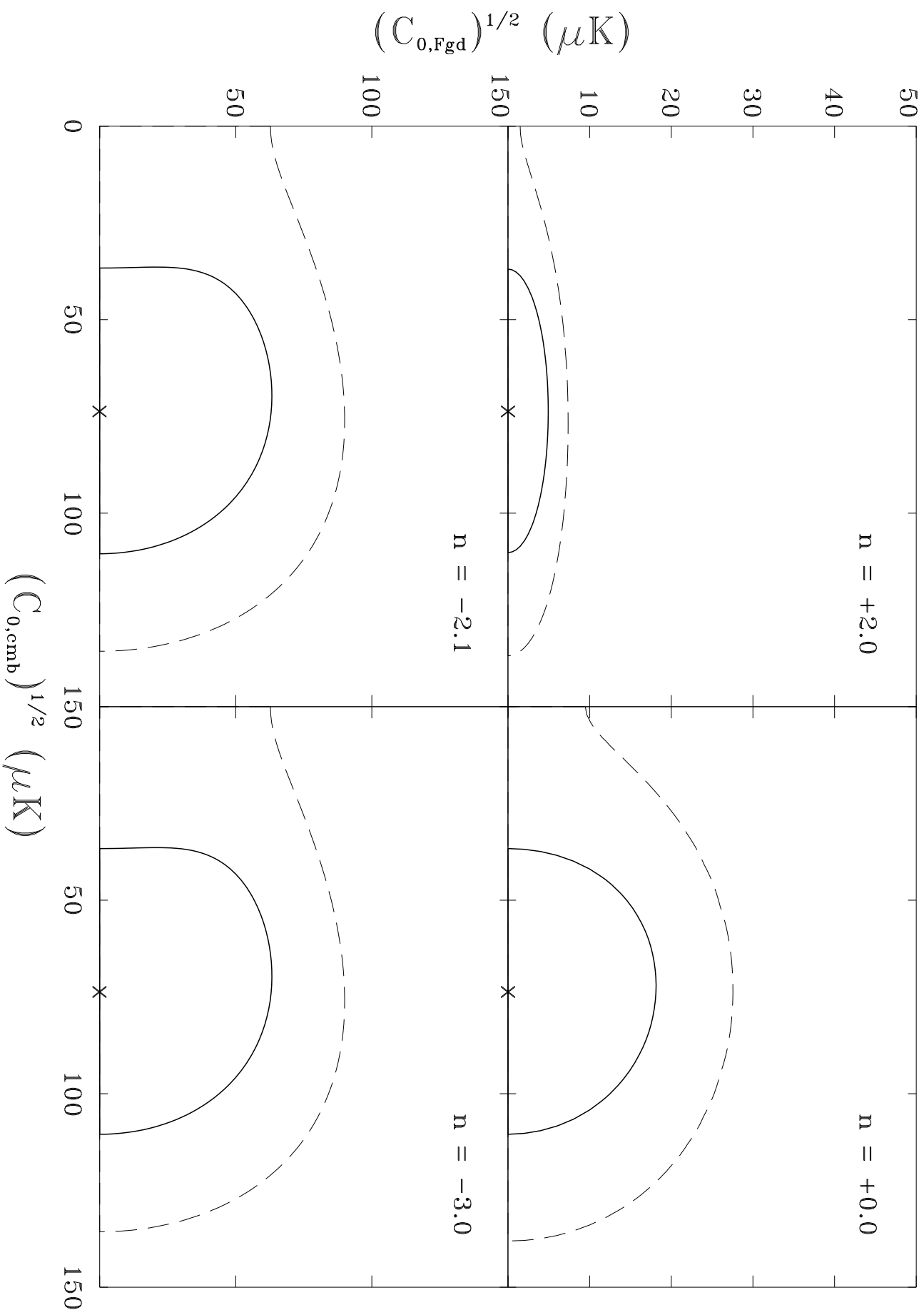


Histogram in percentage









$(C_{0,\text{Fgd}})^{1/2} (\mu\text{K})$

